Stem Cell Reports
Resource
OPEN ACCESS

Enhancer Chromatin and 3D Genome Architecture Changes from Naive to Primed Human Embryonic Stem Cell States

Stephanie L. Battle,[1,2] Naresh Doni Jayavelu,[1,2,5] Robert N. Azad,[1,2,5] Jennifer Hesson,[2,3] Faria N. Ahmed,[1,2] Eliah G. Overbey,[1,2] Joseph A. Zoller,[1] Julie Mathieu,[2,4] Hannele Ruohola-Baker,[2,4] Carol B. Ware,[2,4] and R. David Hawkins[1,2,*]

[1]Division of Medical Genetics, Department of Medicine, Department of Genome Sciences, University of Washington School of Medicine, Seattle, WA, USA
[2]Institute for Stem Cell and Regenerative Medicine, University of Washington School of Medicine, Seattle, WA, USA
[3]Department of Comparative Medicine, University of Washington School of Medicine, Seattle, WA, USA
[4]Department of Biochemistry, University of Washington School of Medicine, Seattle, WA, USA
[5]Co-second author
*Correspondence: rdhawk@uw.edu
https://doi.org/10.1016/j.stemcr.2019.04.004

SUMMARY

During mammalian embryogenesis, changes in morphology and gene expression are concurrent with epigenomic reprogramming. Using human embryonic stem cells representing the preimplantation blastocyst (naive) and postimplantation epiblast (primed), our data in 2iL/I/F naive cells demonstrate that a substantial portion of known human enhancers are premarked by H3K4me1, providing an enhanced open chromatin state in naive pluripotency. The 2iL/I/F enhancer repertoire occupies 9% of the genome, three times that of primed cells, and can exist in broad chromatin domains over 50 kb. Enhancer chromatin states are largely poised. Seventy-seven percent of 2iL/I/F enhancers are decommissioned in a stepwise manner as cells become primed. While primed topologically associating domains are largely unaltered upon differentiation, naive 2iL/I/F domains expand across primed boundaries, affecting three-dimensional genome architecture. Differential topologically associating domain edges coincide with 2iL/I/F H3K4me1 enrichment. Our results suggest that naive-derived 2iL/I/F cells have a unique chromatin landscape, which may reflect early embryogenesis.

INTRODUCTION

Dynamic changes in the epigenome are associated with morphological and gene expression changes during early embryogenesis. Soon after fertilization DNA methylation is actively removed from the paternal genome, passively lost from the maternal genome, and regained in the postimplantation epiblast (Guo et al., 2014). In addition to resetting the DNA methylome, the early embryonic epigenome maintains an open chromatin structure as repressive heterochromatin is gained later over the course of development, lineage commitment, and differentiation (Ahmed et al., 2010; Liu et al., 2004; Sarmento et al., 2004). These changes in histone modification correlate with the hypothesis that a more open chromatin structure is a key aspect of pluripotency and allows embryonic cells to respond to a broad array of developmental signaling cues (Hawkins et al., 2010; Meshorer et al., 2006).

Pre- and postimplantation pluripotent embryonic stem cells (ESCs) provide a system to model epigenomic reprogramming during early embryogenesis and to study changes in pluripotency. In the past few years, several groups described the first set of naive human ESCs (hESCs), whereby primed hESCs or human pluripotent stem cells were induced, or reset, to the naive state (Chan et al., 2013; Gafni et al., 2013; Hanna et al., 2010; Takashima et al., 2014; Theunissen et al., 2014; Valamehr et al., 2014; Ware et al., 2014). Additionally new hESC lines were derived, each under a different naive growth condition (Gafni et al., 2013; Guo et al., 2016; Theunissen et al., 2014; Ware et al., 2014; for review see Ware, 2016). Similar to mouse, naive hESCs exhibit DNA hypomethylation and two active X chromosomes (Gafni et al., 2013; Theunissen et al., 2016; Ware et al., 2014), hallmarks of the preimplantation state.

Given the differences between early human and mouse embryogenesis (Blakeley et al., 2015; Rossant, 2015), naive-derived hESC lines provide an opportunity to study changes that are reflective of early human development and pluripotency. To better our understanding of epigenomic reprogramming as hESCs transition from naive to primed, we present data from whole-transcriptome RNA sequencing (RNA-seq), chromatin immunoprecipitation sequencing (ChIP-seq) for five histone modifications, and topologically associating domains (TADs) from *in situ* DNaseI Hi-C for the naive-derived Elf1 line (Ware et al., 2014) grown in 2i + leukemia inhibitory factor (LIF) + insulin-like growth factor 1 (IGF1) + fibroblast growth factor (FGF) (2iL/I/F). Elf1 cells grown in this culture condition were previously shown to be naive based on gene expression, but in a later stage of development compared with 5iL/A and t2iL + Gö cells, and are more similar to mouse ESCs (mESCs) (Figure 1A) (Moody et al., 2017). We include data from cells that are exiting or transitioning out of the naive state (activin + FGF) and compared our results with data from primed H1 hESCs (Dixon et al., 2012; Hawkins

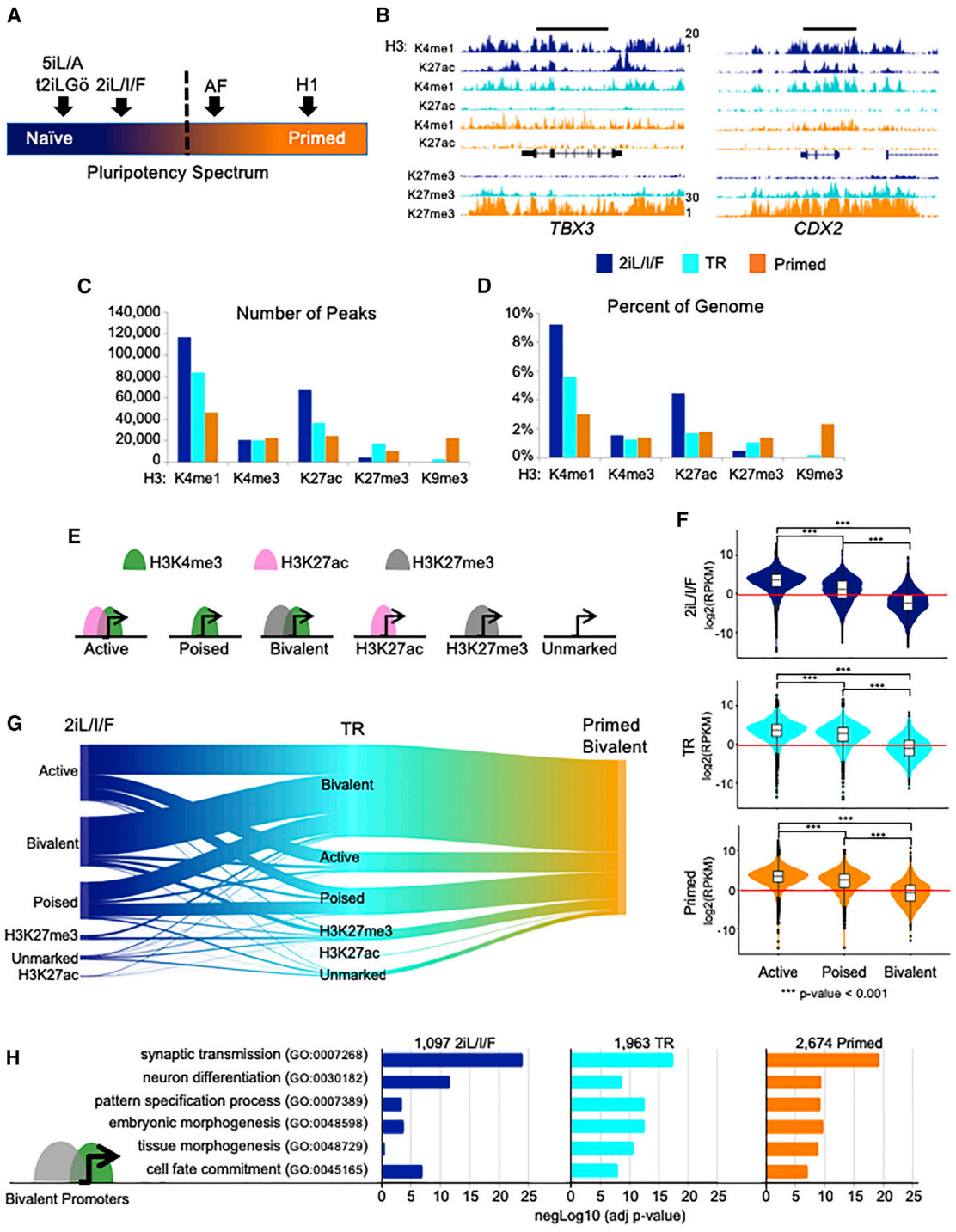

Figure 1. Overview of Chromatin States

(A) Schematic of where 2iL/I/F and other ESCs lie on the pluripotency spectrum. Dashed line represents transition from naive to primed. Adapted from Moody et al. (2017).

(B) Global view of chromatin structure for 2iL/I/F (navy), transitioning (TR; cyan) and primed (orange) hESCs. These colors are used throughout all figures. UCSC Genome Browser images of *TBX3* and *CDX2* gene loci showing enrichment of H3K4me1 (RPKM range 1–20), H3K27ac (RPKM range 1–20), and H3K27me3 (RPKM range 1–30) in 2iL/I/F, transitioning and primed cells.

(C) The number of ChIP-seq peaks called by MACS with FDR cutoff $\leq$0.05.

(legend continued on next page)

et al., 2010). Extensive chromatin remodeling occurs at promoters and enhancer elements as cells transition from naive to primed. Our analysis reveals that 2iL/I/F hESCs have a more open chromatin structure due to large expansions of H3K4me1 and H3K27ac in the genome. Seventy-seven percent of 2iL/I/F enhancers are decommissioned in the primed state. TADs are largely stable between pluripotent states, but our data reveal limited 2iL/I/F-specific shifts in TAD boundaries. Overall, these data provide an extensive view of the epigenome and three-dimensional (3D) genome for hESC states and a model for epigenomic reprogramming during early human embryogenesis.

RESULTS

Gene Expression in 2iL/I/F hESCs

It is currently accepted that pluripotency exists as a spectrum (Wu and Izpisua Belmonte, 2015; Zimmerlin et al., 2017), and 2iL/I/F cells are useful for studying the naive-to-primed transition (Figure 1A). As additional support of their position on the naive spectrum, we tested the presence of naive-specific cell-surface markers previously identified by Collier et al. (2017) using fluorescence-activated cell sorting (FACS). We found that the majority of 2iL/I/F cells expressed naive cell-surface markers CD77 and CD75 (Figures S1A and S1B). We also performed reduced representation bisulfite sequencing (RRBS) to measure the global DNA methylation level in 2iL/I/F cells. 2iL/I/F cells are more methylated than cells grown in the naive 5iL/A condition but hypomethylated compared with primed cells (Figure S1C). 2iL/I/F cells also exist in a metabolic state similar to preimplantation embryos, unlike the glycolytic state of primed cells (Sperber et al., 2015; Zhou et al., 2012). Altogether, this indicates that 2iL/I/F cells have characteristics that are reflective of preimplantation development and *in vitro* naive states. We then performed strand-specific, whole-transcriptome RNA-seq in replicate on Elf1 2iL/I/F, Elf1 transitioning (activin + FGF; referred to as TR) and H1 primed (mTeSR) cells of equal cell numbers (Figures S1D–S1F). We identified differentially expressed genes (DEGs) in a pairwise manner (Figures S1G and S1H). The largest number of DEGs was observed between 2iL/I/F and primed hESCs (Figure S1H and Table S1), signifying just how distinct these cellular states are. Highlighted in Figures S1G and S1H are several genes known to be upregulated in the human preimplantation epiblast (Blakeley et al., 2015; Yan et al., 2013) and other key genes of interest.

We identified gene ontology (GO) categories and KEGG pathways for 2iL/I/F DEGs, which were significantly enriched for embryo development and pluripotency signaling pathways along with other pathways important during preimplantation development (Figures S1I and S1J). In particular, genes in the transforming growth factor β (TGF-β) pathway were found to be upregulated in 2iL/I/F cells, including *LEFTY1*, *SMAD3*, and *NODAL*. The TGF-β pathway was shown to be important for maintenance of *NANOG* in the human epiblast, whereas inhibition of this pathway has insignificant effects on mouse embryos (Blakeley et al., 2015). The PI3K-AKT signaling pathway was also enriched, and is known to promote ESC self-renewal through inhibition of the ERK signaling pathway (Chen et al., 2012). The WNT signaling pathway was enriched for naive upregulated genes including *WNT8A*, *WNT5B*, and *TCF7* (Sperber et al., 2015). A number of terms associated with embryonic development and morphogenesis were enriched for 2iL/I/F upregulated genes.

We identified cell-type-specific genes in the different hESC stages by applying a cutoff of an RPKM (reads per kilobase per million) value greater than or equal to 2 in one cell type and less than 1 in the other two cell types (Figure S2A). Using this cutoff we determined 429 2iL/I/F-specific genes, 229 TR-specific genes, and 333 primed-specific genes. Compared with the primed states, 2iL/I/F-specific genes were enriched for GO terms associated with morphogenesis and pattern specification (Figure S2A). This is due, in part, to the many *HOX* genes that are uniquely expressed in 2iL/I/F hESCs and not in transitioning or primed cells. Primed cells were enriched for terms associated with extracellular communication and protein/histone demethylation.

A recent report showed that the transposable element (TE) transcriptome can be used as a state-specific signature in hESCs (Theunissen et al., 2016). 2iL/I/F and primed hESCs segregate when clustered on the top 1,000 highest expressed TEs (Figure S2B). We see that HERVK and LTR5 are upregulated in 2iL/I/F cells while HERVH and LTR7 are upregulated in primed. Lastly, we compared upregulated genes with human embryo RNA-seq data from Yan et al. (2013). We find that a similar percentage of

(D) The percentage of genome covered by each histone modification.
(E) Cartoon showing different categories of promoter states.
(F) Violin plots showing the distribution of RPKM values of NNGs of active, poised, and bivalent promoter peaks in each cell type. p values for pairwise comparisons are computed using two tailed t tests with pooled SD. p values are adjusted with Benjamini-Hochberg method. ***$p < 0.001$.
(G) Sankey plot of primed bivalent gene promoters and their origins from the 2iL/I/F state.
(H) Significance level of GO terms from bivalently marked gene promoters.

upregulated genes from 2iL/I/F and primed are expressed in pre-zygotic genome activation stages, while 2iL/I/F hESCs share more upregulated genes with the post-zygotic genome activation (ZGA) embryo than primed (Figure S2C). This strengthens reports that Elf1 cells are a good representative model of the preimplantation stage of human development (Moody et al., 2017; Sperber et al., 2015; Ware et al., 2014).

Global Chromatin Features of 2iL/I/F hESCs

To assess global chromatin dynamics between the cellular states, we performed ChIP-seq on five histone modifications from 2iL/I/F and transitioning cells (Table S2), and used data previously generated in H1 hESCs for the primed state (Hawkins et al., 2010). These modifications include H3K4me3 for Pol II-bound promoters, H3K4me1 for enhancers, H3K27ac for active regions, H3K27me3 for Polycomb-repressed regions, and H3K9me3 for heterochromatin. All five modifications along with ChIP inputs were sequenced in duplicates for both Elf1 2iL/I/F and Elf1 transitioning cells for a total of >270 million and >213 million sequencing reads, respectively (Table S2).

We inspected genes with known expression differences during early embryogenesis through the blastocyst/epiblast stage to ensure our chromatin maps reflect known changes during differentiation from naive to primed. *TBX3* was shown to be expressed in naive ESCs and human epiblasts (Blakeley et al., 2015). The *TBX3* locus exhibits high levels of H3K4me1 and H3K27ac in naive hESCs, a reduction of H3K27ac in the transitioning state, followed by a reduction of H3K4me1 and a gain of H3K27me3 in primed hESCs (Figure 1B). *KLF2*, which was shown not to be expressed in human naive cells (Blakeley et al., 2015), lacks the H3K27ac modification in all three hESC stages (Figure S3A). *CDX2* has active histone modifications in naive hESCs but transitions to a loss of acetylation and gain of H3K27me3 in primed hESCs (Figure 1B). CDX2 protein has been shown to be present after blastocyst formation in human embryos and overlaps OCT4 protein in preimplantation embryos (Niakan and Eggan, 2013). Expansion of H3K27me3 domains are also shown at the HOXA locus as hESCs move from naive to primed (Figure S3B). Next, we asked whether these trends observed at specific loci held true genome wide.

Comparisons across cell types reveal a genome-wide depletion of repressive histone modifications in 2iL/I/F cells (Figures 1C and 1D). H3K27me3 repressed regions are more abundant and broader in primed than in 2iL/I/F cells, covering ~1.4% of the genome in primed cells compared with 0.5% in 2iL/I/F (Figures 1D and S3C), which we previously showed is linked to metabolic differences between the cell states (Sperber et al., 2015). H3K9me3 heterochromatin regions, which are sparse in primed cells (Hawkins et al., 2010), are further depleted in transitioning and 2iL/I/F cells (Figures 1C, 1D, and S3D; Table S3). There is a notable abundance of H3K4me1 regions in 2iL/I/F hESCs (Figure 1C and Table S3). Over 9% of the 2iL/I/F genome is marked by H3K4me1, 3-fold more than primed cells and 1.7-fold more than transitioning cells (Figure 1D and Table S3). Monomethylation is present in larger domains, reaching sizes of over 30 kb in transitioning cells and over 50 kb in 2iL/I/F cells (Figure S3E). Acetylation is also more enriched in 2iL/I/F cells with 3-fold more peaks than primed, which is similar to H3K27ac in naive 5iL/A cells where it also covers ~4% of the genome (Ji et al., 2016). Similar to H3K4me1, broad H3K27ac domains can reach over 50 kb (Figures 1C, 1D, and S3F; Table S3). We found H3K4me3 to be the most stable mark although cell-specific peaks exist (Figures 1C, 1D, and S3G). The trends for histone modifications also hold true for a second primed line, H9 (Figure S3H).

Promoter Transitions as hESCs Exit the Naive State

We investigated how DEGs were reflected through promoter chromatin states using >19,000 GENCODE defined autosomal protein coding genes. Over 12,000 promoters are marked with H3K4me3 (Figure S4A). We divided promoters into six categories: (1) active—H3K4me3 and H3K27ac; (2) poised—H3K4me3 only; (3) bivalent—H3K4me3 and H3K27me3; (4) H3K27ac—H3K27ac only; (5) H3K27me3—H3K27me3 only; and (6) unmarked—lacking all three modifications (Figures 1E and S4B). Although the largest percentages of gene promoters remain static as either active or unmarked across all three stages, many promoters change chromatin state (Figure S4C), which exemplifies the dynamic nature of the epigenome. To illustrate that chromatin patterns coincide with general trends of expression, we plotted the RPKM values of genes with active, poised, and bivalent promoters. As expected, genes with active promoters had overall higher expression levels than genes with promoters in the other two categories (Figure 1F).

We observed an increase in bivalent gene promoters from 2iL/I/F to primed cells (1,097 versus 2,674), and determined from which epigenetic states the primed bivalent promoters arose. Roughly 60% of primed bivalent promoters are bivalent in transitioning cells, and of those, their promoter states are split between active (42%), bivalent (32%), and poised (20%) in 2iL/I/F hESCs (Figure 1G). Of the ~7% of 2iL/I/F active gene promoters that become bivalent in transitioning cells, these genes were enriched for GO terms such as morphogenesis and WNT signaling, and included genes such as *HOXA1*, *HOXA4*, *HOXD8*, and *ZEB1*. 2iL/I/F bivalent genes fall into categories involving GO terms for synaptic transmission, ion transport, and neuron differentiation (Figure 1H). Thus, it

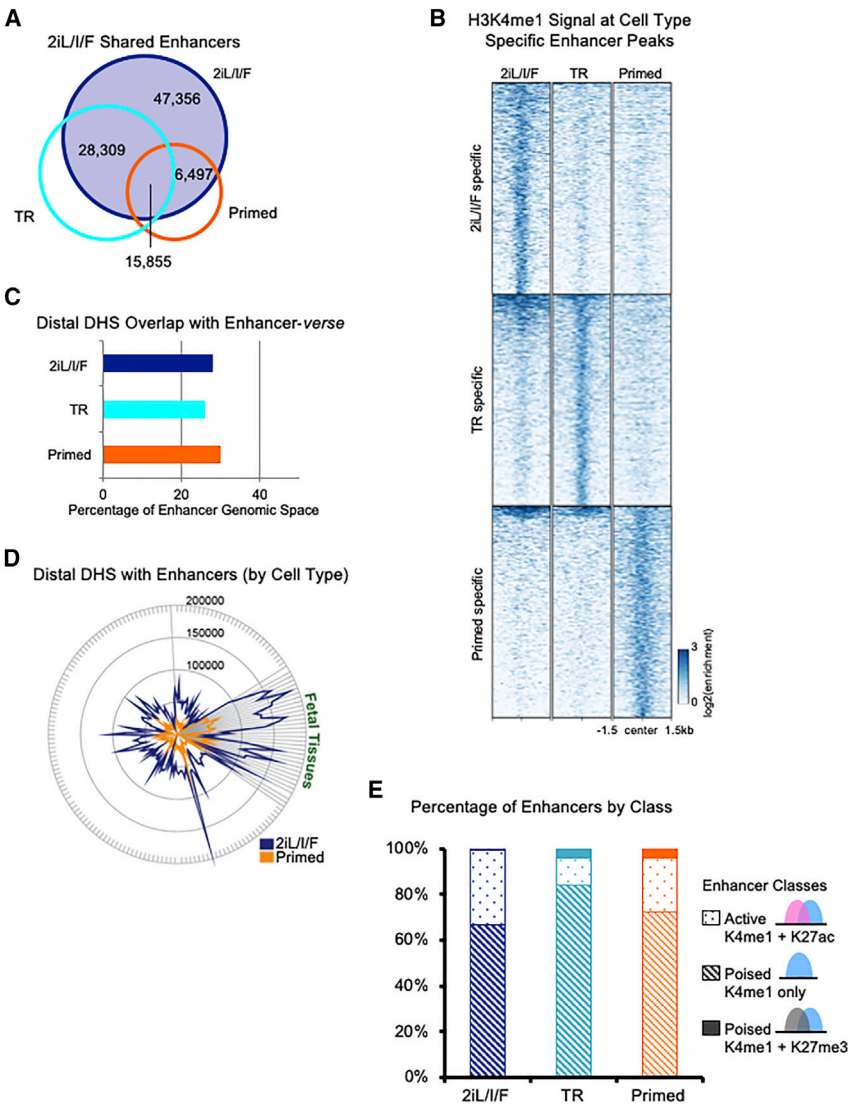

Figure 2. 2iL/I/F Enhancer Repertoire

(A) Venn diagram of 2iL/I/F (navy) enhancers overlapped with transitioning (cyan) and primed (orange) enhancers.

(B) Heatmap of H3K4me1 normalized ChIP-seq signal centered at cell type-specific enhancers in a 3-kb window.

(C) Percentage of hESC H3K4me1 genomic space, i.e., number of base pairs, occupied by ENCODE DNase hypersensitive sites (DHS) from 177 cell types.

(D) Number of ENCODE DHS from 177 cell types overlapping with 2iL/I/F and primed H3K4me1 enhancers.

(E) Percentage of active (H3K4me1 + H3K27ac) and poised (H3K4me1 only or H3K4me1 + H3K27me3) enhancer states in each cell type.

appears that the neural lineage is one of the first lineages to be bivalently marked in 2iL/I/F cells and further suggests that naive hESCs may be an excellent model for further investigation of the establishment of Polycomb-repressive regions in the early epigenome.

Enhancers in 2iL/I/F Cells

Enhancer elements are *cis*-acting regulatory sequences that control gene expression via interaction with transcription factors and promoters. We defined enhancers as H3K4me1 peaks lacking overlap with H3K4me3 (Table S3) (Heintzman, 2007; Heintzman, 2009). Investigation of the enhancer landscape across hESC states revealed that 2iL/I/F cells harbor the most cell-type-specific enhancers (>47k; Figures 2A and 2B), while transitioning and primed cells had roughly the same number of unique enhancers at ~17k and ~14k, respectively (Figures 2B, S5A, and S5B). Sixty-four percent of transitioning enhancers and 55% of primed enhancers are marked in the 2iL/I/F state (Figures S5A and S5B). We asked whether the expansion of 2iL/I/F H3K4me1 was random or occurred at known regulatory elements. Using DNase I hypersensitive sites (DHS) data from 177 ENCODE cells (ENCODE Project Consortium, 2012), we found 25%–30% of the H3K4me1-marked genome (enhancer-verse) to be hypersensitive in each of our pluripotent cell types (Figure 2C). Of the 177 cell and tissue types, fetal tissues had the largest collection of DHS overlapping 2iL/I/F enhancers (Figure 2D and Table S4). Additionally, over 92% of the enhancer regions (quantified by number of bases) covered by 2iL/I/F H3K4me1 peaks are utilized as enhancers in 127 Roadmap Epigenome Project cell types, as indicated by H3K4me1

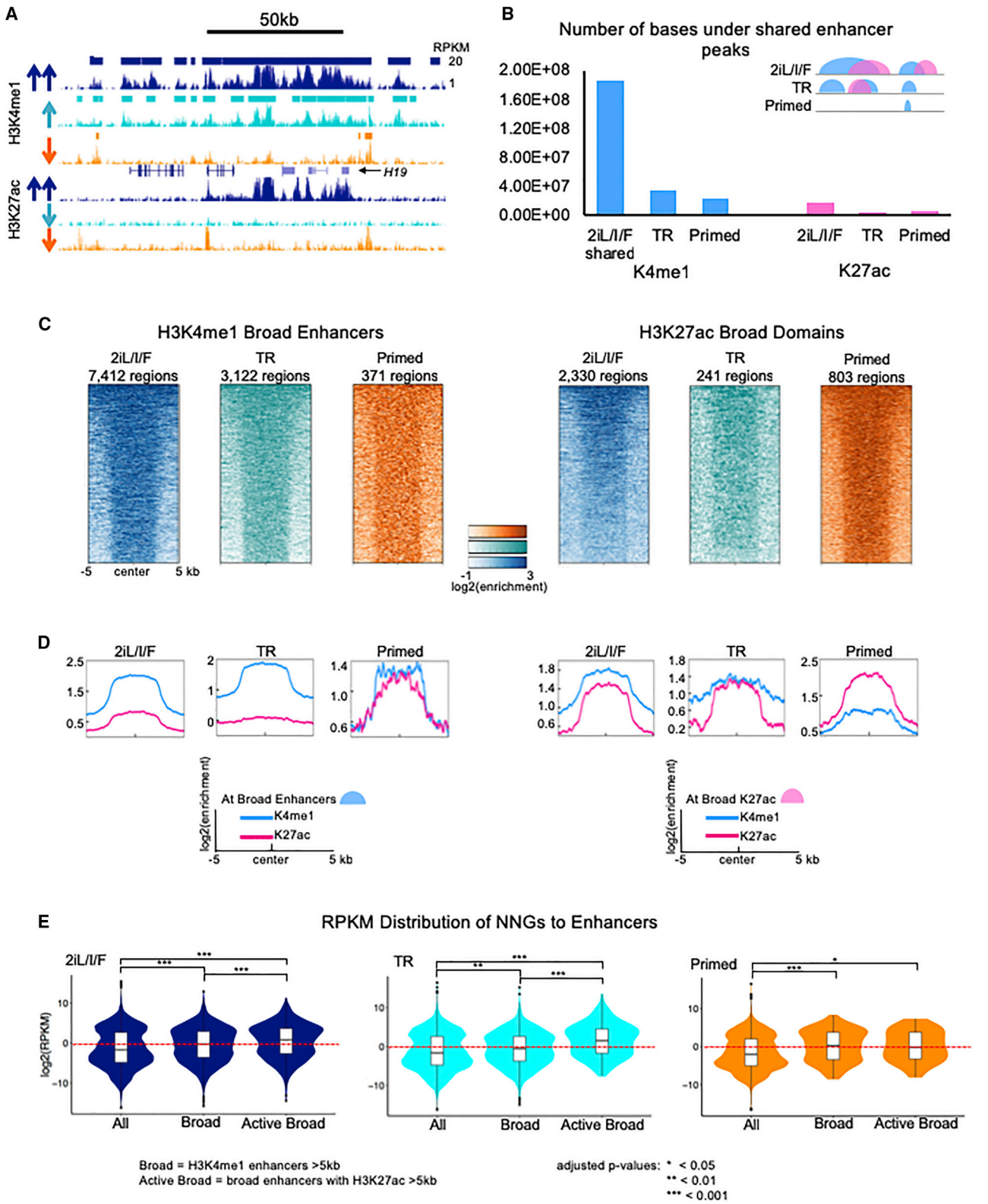

(legend on next page)

(Figures S5C and S5D). Single-cell RNA-seq data from early human embryogenesis (Yan et al., 2013) indicate that 92% of annotated transcription factors (Zhang et al., 2015) are expressed by the late blastocyst stage (Figure S5E). Their expression provides a plausible means for aiding the localization of H3K4me1 to known enhancers.

Enhancer elements can exist in distinct chromatin states, or classes, that indicate whether they are active or poised (Figures 2E and S5F) (Creyghton et al., 2010; Hawkins et al., 2011; Rada-Iglesias et al., 2011). We characterized differences in the classes of enhancers in each hESC state. We defined active enhancers as regions having H3K4me1 and H3K27ac and poised enhancers as regions with either H3K4me1 only or H3K4me1 and H3K27me3. In all three stages of pluripotency, the majority of enhancers are in the H3K4me1 only poised state (67%, 84%, and 73% in 2iL/I/F, transitioning, and primed cells, respectively; Figure 2E). There is an increase of H3K27me3 containing poised enhancers moving from 2iL/I/F to primed (1%–4%; Figure 2E), which correlates with the increase of H3K27me3.

Our comparative analysis of enhancers indicates that both active and H3K4me1 only poised enhancers are largely decommissioned as 2iL/I/F hESCs transition to the primed state (Figure 3A). When assessing overlapping H3K4me1 peaks across hESCs, we see that the chromatin-marked genomic space of 2iL/I/F enhancers is greatly reduced in primed cells (Figures 3A and 3B). This is exemplified at the *H19* locus, where broad enhancers are shorter and broken up in the transitioning state, and most have disappeared by primed state (Figure 3A). This process happens in a stepwise manner, as is evidenced by the loss of acetylation as cells exit the 2iL/I/F state followed by the gradual loss H3K4me1. We observed this globally and at shared 2iL/I/F enhancer regions (Figures 1B, 1C, 3A, and 3B). This introduces an alternative view of development compared with previous studies showing that poised enhancers gain acetylation following differentiation and were often enriched near genes that became activated later in development (Creyghton et al., 2010; Hawkins et al., 2011; Rada-Iglesias et al., 2011). By using 2iL/I/F hESCs as a model, we can infer that not only is H3K4me1 likely maintaining open chromatin to aid in the pluripotency phenotype, but that a substantial fraction of enhancers in the human genome are premarked early during embryogenesis and subsequently decommissioned during priming.

Broad Enhancer Domains in the 2iL/I/F Epigenome

Super (Whyte et al., 2013) and stretch (Parker et al., 2013) enhancers, which are largely based on H3K27ac, were originally identified in primed ESCs. These regions were shown to upregulate nearby and cell-specific genes and were stronger than conventional enhancers. We asked to what degree these regions were present in 2iL/I/F hESCs. To identify both broad H3K4me1 and H3K27ac domains, we identified regions $\geq$5 kb in all cell types (Figure 3C). The H3K4me1 broad enhancers are almost 20-fold more abundant in the 2iL/I/F epigenome compared with the primed hESC stage (7,412 in 2iL/I/F hESCs compared with 371 in primed) with an average size of 8.1 kb compared with 6.1 kb in primed (Figures S5G and S5H). The number of broad enhancers steadily declines as hESCs transition from 2iL/I/F to primed. We observed the same trend with H3K27ac broad domains (2,330 in 2iL/I/F compared with 803 in primed), although the number of broad H3K27ac domains in 2iL/I/F cells is 3-fold less than the number of H3K4me1 broad enhancers (Figure S5G). For perspective, we looked for broad H3K4me3 peaks, and found them to be limited across the different hESC stages (Figure S5G).

Next, we determined whether H3K4me1 broad enhancers and H3K27ac broad domains occupy the same genomic space. The average number of bases contained within the overlap of broad H3K4me1 and H3K27ac domains is over 70% of the average length of each domain (Figure S5H). Over 78% of broad H3K27ac domains in 2iL/I/F cells are found within H3K4me1 broad enhancers (Figure S5I). In the 2iL/I/F and primed states 87% and 71% of H3K4me1 broad enhancers, respectively, contained some overlap with H3K27ac, indicating that they are active

Figure 3. 2iL/I/F Enhancers Are Decommissioned but Active in Other Cell Types

(A) UCSC Genome Browser image illustrating loss of H3K27ac, followed by loss of H3K4me1 at the *H19* locus as cells move from 2iL/I/F (navy), to transitioning (cyan), to primed (orange); RPKM range 1–20 for each track. This region also contains a broad enhancer domain in 2iL/I/F hESCs. Enhancer peak calls are represented as bars above the H3K4me1 track.

(B) Number of bases under peaks overlapping shared (all three cell types) 2iL/I/F enhancers. H3K27ac is reduced greatly in the transitioning genome, then there is a great reduction in H3K4me1.

(C) Heatmaps of H3K4me1 and H3K27ac normalized ChIP-seq signal at broad enhancer regions ($\geq$5 kb).

(D) Histograms of average H3K4me1 and H3K27ac normalized ChIP-seq signal at all broad enhancers or broad H3K27ac domains.

(E) Violin plots showing the distribution of RPKM values of nearest neighboring genes of all enhancers, broad enhancers (H3K4me1 $\geq$5 kb), or active broad enhancers (H3K4me1 $\geq$5 kb overlapping H3K27ac $\geq$5 kb) in each cell type. p values for pairwise comparisons are computed using two-tailed t tests with pooled SD. p values are adjusted with Benjamini-Hochberg method. *$p < 0.05$; **$p < 0.01$; ***$p < 0.001$.

enhancers (Figures 3D and S5I). The average ChIP-seq signal for H3K4me1 is high at H3K27ac broad domains in all cells except primed hESCs (Figure 3D). The active state of broad enhancers is supported by the distribution of expression values of nearest neighboring genes (NNGs) (Figure 3E). Only in the primed state are there more broad H3K27ac domains than H3K4me1 domains, and the difference in the expression distribution of NNGs at broad enhancers versus active broad enhancers in primed cells was the only comparison not found to be significant (Figure 3E). This may explain why H3K27ac was originally associated with "super/stretch" enhancers, as most broad H3K4me1 domains are found at broad H3K27ac domains and broad H3K27ac domains are more abundant. However for naive pluripotency the frequent occurrence of H3K4me1 and H3K27ac broad domains, and the observation that broad H3K27ac domains lie within broad H3K4me1 enhancers, provides an additional means of giving the genome its "open structure."

2iL/I/F hESCs Enhancers in Different Growth Conditions

To determine whether the expansion of H3K4me1 in the 2iL/I/F epigenome was indicative of the naive state and independent of a single growth condition or cell line, we grew three lines in 4i (2i + p38 kinase inhibitor + JNK inhibitor) + LIF + IGF1 + FGF (4iL/I/F [Sperber et al., 2015]): Elf1, H1 reset to naive, and the naive-derived LIS1 line (Gafni et al., 2013) (Figure S6A). The LIS1 line grew slightly better in 4iL/I/F compared with the original growth conditions. To determine whether growth conditions or genetic background had an effect on the enhancer landscape, we compared the enhancer profiles from H3K4me1 ChIP-seq data across cell types and conditions. Overall, all naive cells have a similar enhancer profile (Figure 4A). Cells grown in 4iL/I/F exhibit a stronger enhancer signal at Elf1 2iL/I/F-specific enhancers (Figures 4B and 4C), and less enrichment at primed- and transitioning-specific enhancers (Figures 4B and S6B). Principal component analysis (PCA) of gene expression data shows a clear separation between naive and primed cells (Figure S6C). PCA of H3K4me1 signal reveals that all lines grown in 4iL/I/F are largely indistinguishable, and most similar to 2iL/I/F (Figure 4D). Our analysis suggests that 2iL/I/F enhancers do not vary greatly in 4iL/I/F conditions, although 2iL/I/F hESCs have some distinct H3K4me1 features. The acquired expansion upon resetting primed H1 cells to 4iL/I/F may suggest that this epigenetic feature is necessary for maintenance in the naive state. Further experiments will be needed to confirm this hypothesis. Additionally, we find that one-third of H3K27ac peaks in 5iL/A reset hESCs(Ji et al., 2016) are also present in 2iL/I/F hESCs (Figure S6D), highlighting the epigenetic changes that must occur as cells transition through the spectrum of pluripotency, eventually becoming primed.

3D Genome Architecture in 2iL/I/F hESCs

Genome architecture is an important component of gene regulation. TADs identified in primed hESCs proved to be surprisingly stable upon differentiation to distinct cell types despite diverse changes to chromatin structure (Dixon et al., 2015). However, domain-scale 3D genome architecture is still missing for the naive state. To characterize TADs in hESCs at the naive spectrum of pluripotency, we generated deeply sequenced *in situ* DNase Hi-C maps (Deng et al., 2015) in Elf1 2iL/I/F (Figure S7A), which exhibited characteristic reductions in contact frequency as a function of linear distance between two loci (Figure 5A). We processed raw Hi-C read pairs produced from H1 primed hESCs (Dixon et al., 2012, 2015) and compared the architectural features identified in each cell type at 40-kb resolution. A total of 6,119 TADs were identified in 2iL/I/F hESCs and 5,822 TADs in primed hESCs (Figure S7B), consistent with previous observations in primed hESCs (Shin et al., 2016). We defined boundaries as regions between two adjacent TADs and found that 7.3% and 6.2% of boundaries were greater than 40 kb in 2iL/I/F and primed cells, respectively (Figure S7C). To provide confidence in our TAD calls, we calculated insulation scores at each Hi-C bin (Crane et al., 2015; Giorgetti et al., 2016). The insulation score represents how insulated each bin is from TAD boundaries. It is expected that TAD boundaries occur at the valleys/minima of insulation scores, and TAD centers occur at the peaks/maxima. We found that boundary insulation scores were significantly different from TAD center scores (Figure 5B), providing high confidence to our defined TAD regions.

Overall, TAD size distributions are similar (Figure 5C, first panel), with means of 420 kb in 2iL/I/F and 444 kb in primed. We observed 2,024 TADs whose genomic coordinates are identical at 40-kb resolution while the remaining overlapping TADs differ by at least 40 kb (Figure 5C, second panel). We could detect differences in TAD boundaries as illustrated by 2iL/I/F-specific boundaries exhibiting an enrichment of primed Hi-C signal (Figure 5D). The enrichment of primed signal at 2iL/I/F-specific boundaries confirms that this is not a boundary in primed cells. We asked whether the higher number of 2iL/I/F Elf1 TADs may be due to technical differences of our *in situ* data. We found that some H1 TADs were split into two or more Elf1 TADs, which accounts for an "extra" 427 Elf1 TADs (Figure S7D). The average overlap between 2iL/I/F and primed TADs is 319 kb, suggesting that while some difference exist in TAD structure, the overall TAD structure remains intact between the 2iL/I/F and primed states (Figure S7E), To confirm that our *in situ* DNaseI Hi-C data are accurately

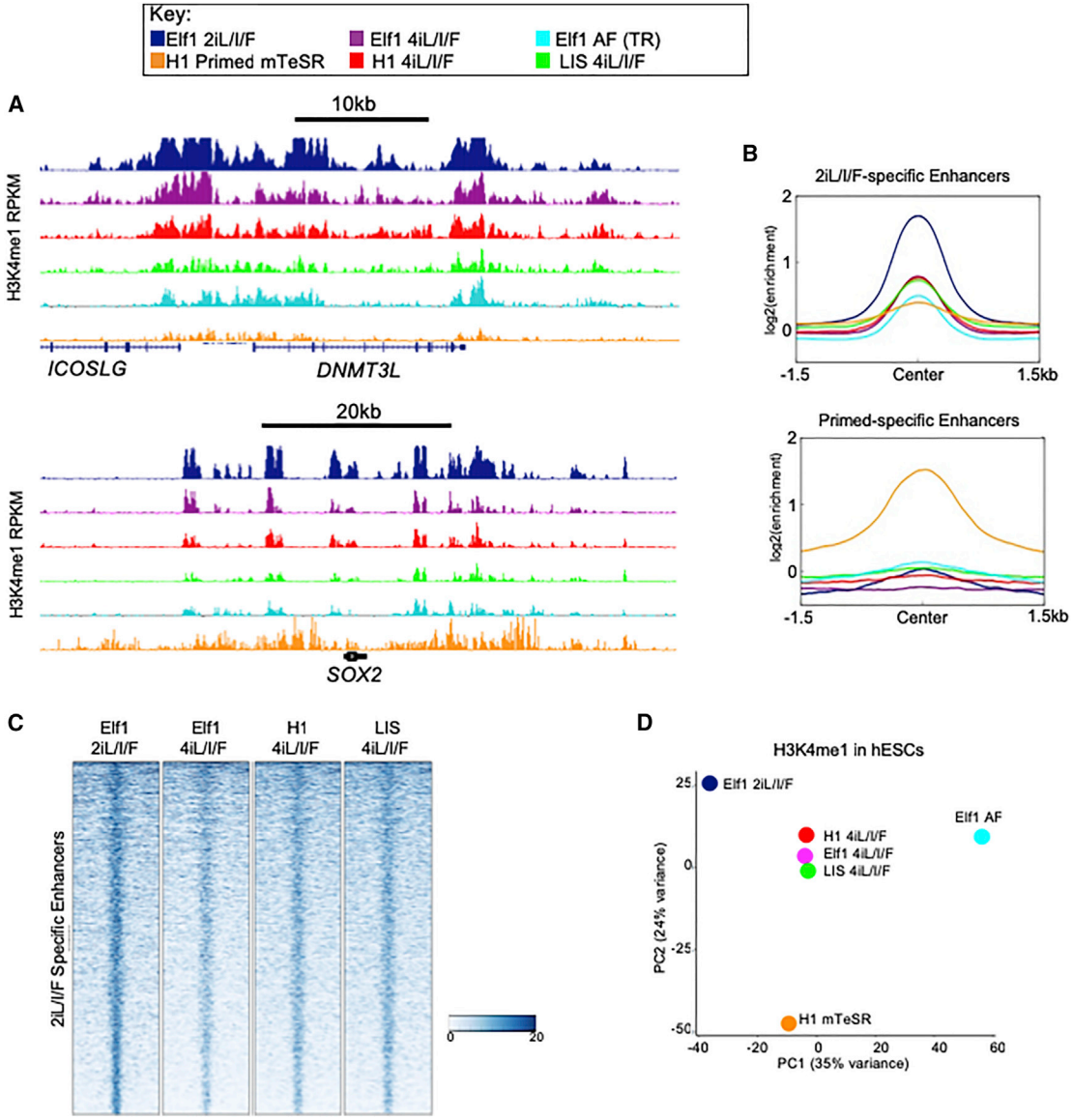

Figure 4. 2iL/I/F Enhancers from Various 2iL/I/F Culture Conditions

ChIP-seq of naive cells grown in different culture conditions including Elf1 2iL/I/F (navy), Elf1 4iL/I/F (purple), Elf1 AF (transitioning; cyan), primed H1 mTeSR (orange), H1 4iL/I/F (red), and LIS1 4iL/I/F (green).

(A) H3K4me1 enrichment in different growth conditions at *DNMT3L* and *SOX2* loci.

(B) Average ChIP-seq signal at 2iL/I/F-specific enhancers (top panel) and primed-specific enhancers (bottom panel).

(C) Heatmap of H3K4me1 ChIP-seq signal at 2iL/I/F-specific enhancers, defined as not in TR or primed. Scale is RPKM.

(D) PCA of top 500 10-kb bins of H3K4me1 with largest variance.

capturing the 3D structure of the naive genome, we utilized cohesin chromatin interaction analysis by paired-end tag sequencing (ChIA-PET) and CTCF ChIP-seq data from primed and reset naive hESCs, which previously revealed changes in looping structures (Ji et al., 2016). Most TADs have a CTCF binding site near their boundaries. We asked whether the reset naive CTCF ChIP-seq signal was also enriched at our 2iL/I/F-derived hESC TAD boundaries. Indeed, we found the CTCF signal to be enriched near our 2iL/I/F boundaries and that this enrichment was present in both our 2iL/I/F and primed hESCs (Figure 5E). This may have been expected, as Ji et al. (2016) found that 80% of CTCF binding sites were shared between their reset naive and primed hESC lines.

We also determined whether the cohesin ChIA-PET data could additionally validate our naive TAD boundary calls,

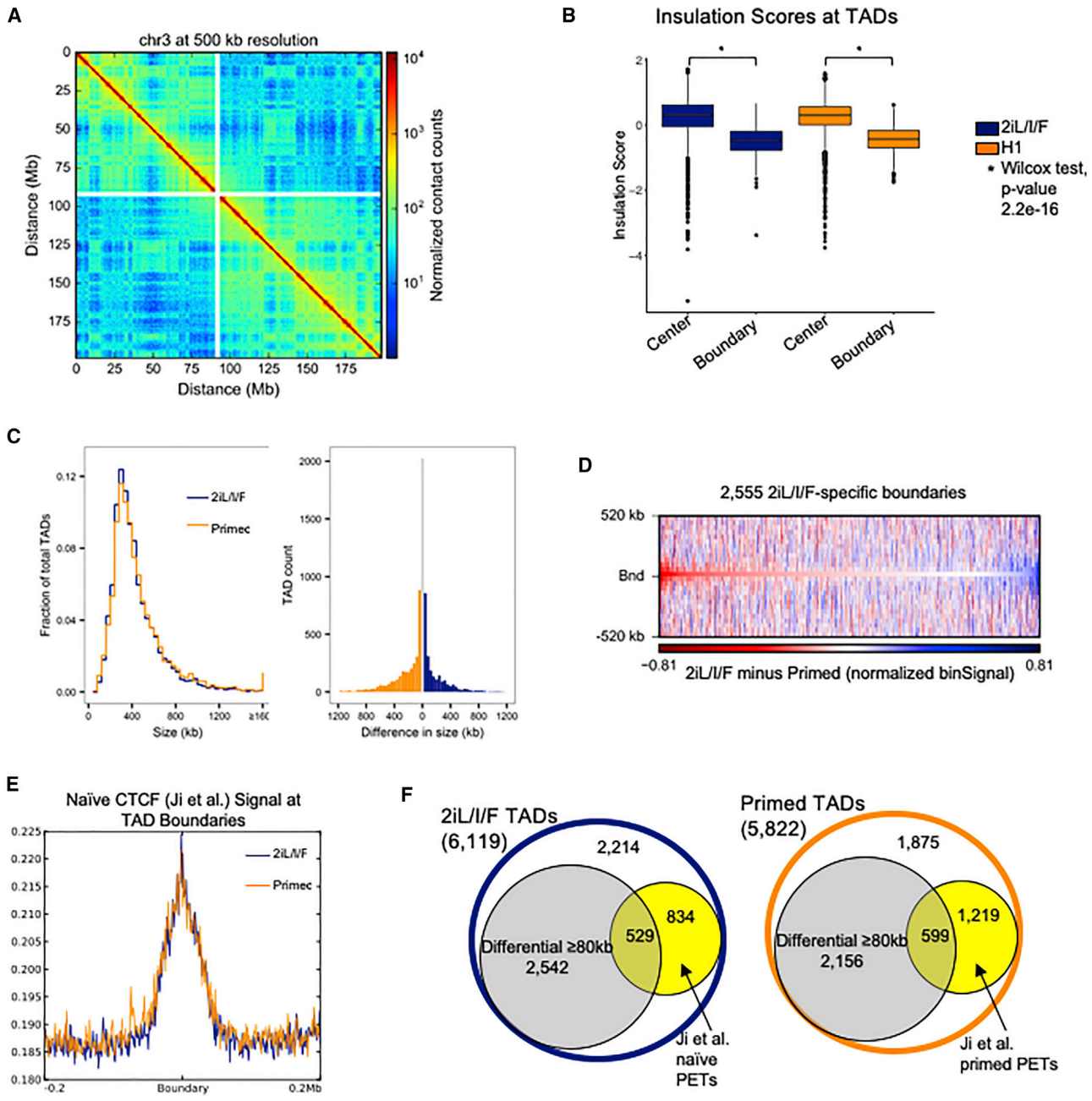

Figure 5. 3D Genome Architecture in 2iL/I/F hESCs

(A) Hi-C contact heatmap of chromosome 3 in 2iL/I/F cells at 500-kb resolution.

(B) Box plots of the insulation scores at all TAD centers and boundaries for both 2iL/I/F and primed cells. p values are computed using individual Wilcoxon signed-rank tests.

(C) Global size distributions of TADs within 2iL/I/F and primed cells (left panel) and size differences of overlapping TADs (40-kb bin resolution) in 2iL/I/F and primed cells (right panel).

(D) Differential heatmap of 2iL/I/F minus primed Hi-C. Negative (red) values indicate a stronger bin signal in primed cells relative to 2iL/I/F cells.

(E) Naive CTCF ChIP-seq signal from Ji et al. (2016) centered at 2iL/I/F TAD boundaries.

(F) Number of TADs or differential TADs with cohesin ChIA-PETs within 80 kb of boundary.

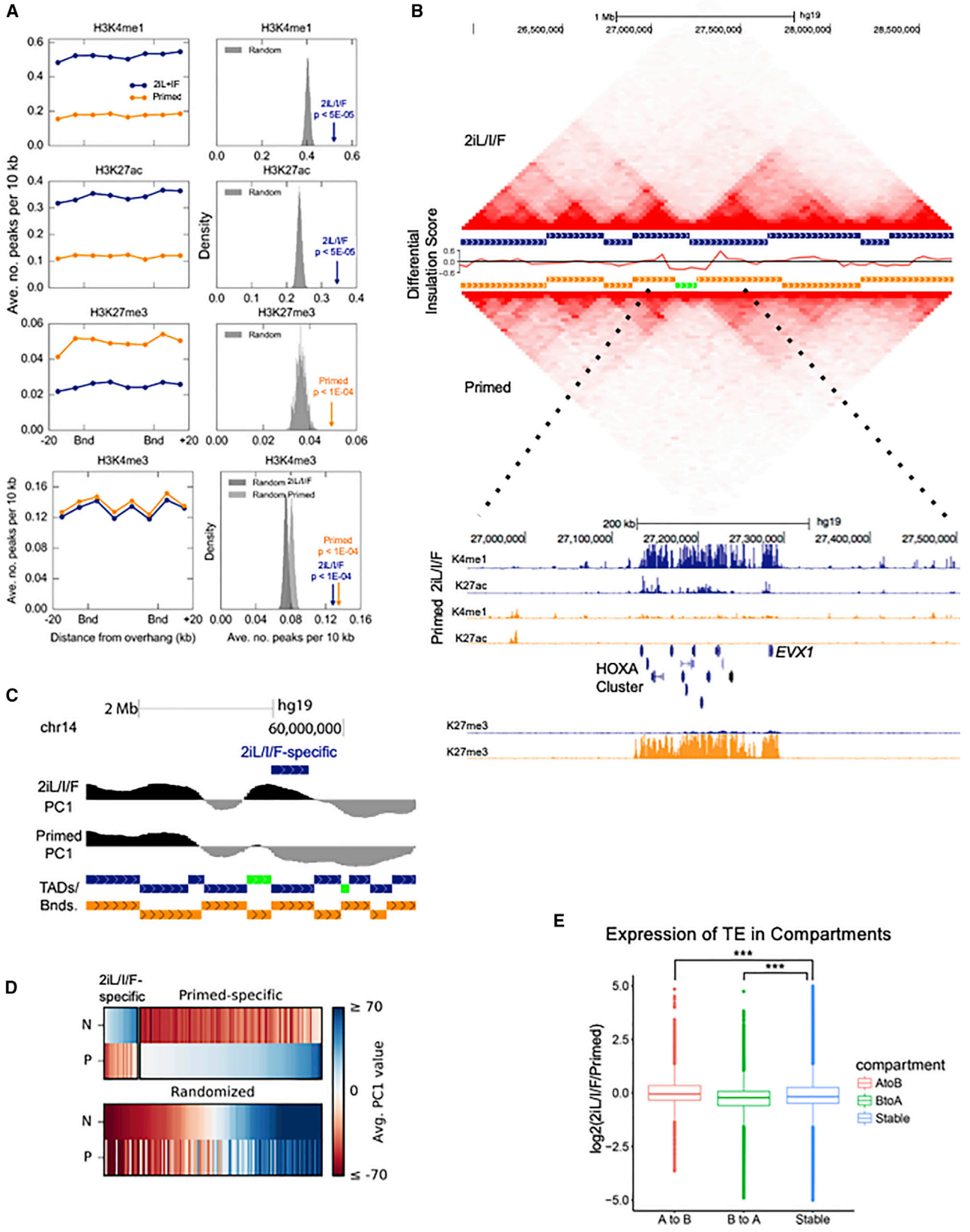

(legend on next page)

since it was shown to recapitulate Hi-C TADs in H1 primed hESCs (Ji et al., 2016). An overlap analysis with cohesin PETs yielded 1,363 2iL/I/F and 1,818 primed TADs with at least one PET, from the respective cell type, whose termini are located within 40 kb of each boundary of a given TAD (Figure 5F). This corresponds to 22% of our 2iL/I/F TADs having a naive PET and 31% of primed TADs having a primed PET within 40 kb of the TAD boundary. We examined whether any of the PETs were localize at differential TAD boundaries, focusing on those boundaries in 2iL/I/F that are 80 kb or greater from the boundary in primed. Of 1,363 PETs near a 2iL/I/F boundary, 529 (39%) are near a 2iL/I/F differential TAD (Figure 5F). Although the authors note that their ChIA-PET data were undersaturated, these data confirm some of the structural differences observed in the 2iL/I/F 3D genome.

We investigated whether there was a relationship between higher-order chromatin structure at differential TAD boundaries and changes in chromatin modifications. We observe a significant enrichment for H3K4me1 and H3K27ac across differential TAD boundaries in 2iL/I/F relative to random (2iL/I/F H3K4me1 and H3K27ac $p < 5 \times 10^{-5}$), and a similar enrichment for primed H3K27me3 ($p < 1 \times 10^{-4}$) (Figure 6A). A clear example illustrating these differences in TAD and chromatin structure is the HOXA cluster, where a broad boundary spans the HOXA cluster in primed hESCs and is enriched for H3K27me3 (Figure 6B). The 2iL/I/F TAD to the left of the primed boundary is extended across the cluster and marked by H3K4me1 and H3K27ac. As mentioned previously, HOXA genes are expressed in 2iL/I/F cells. We asked whether there was a significant difference in the TAD structure around the HOXA locus between 2iL/I/F and primed cells. To do this we calculated the differential insulation scores by comparing the 2iL/I/F and primed insulation scores. The differential insulation score represents the differential TAD structure between two conditions. We observed that there was a noticeable drop in the differential insulation score at the HOXA locus, confirming that the TAD structure at the HOXA locus is different between 2iL/I/F and primed cells (Figure 6B).

Finally, to compare the spatial organization of chromatin within the nuclei of 2iL/I/F and primed hESCs, we partitioned the genome into active and inactive (A/B) compartments by performing a PCA of each intrachromosomal contact matrix (Dixon et al., 2015; Lieberman-Aiden et al., 2009). Compartments identified using the first principal component (PC1) ranged in size from 40 kb to over 49 Mb in both cell types, with means of 3.6 Mb in 2iL/I/F cells and 3.4 Mb in primed. An overwhelming majority of compartments are static, with only 23 switching from being active in 2iL/I/F cells to inactive in primed (A to B), and 124 switching from being active in primed cells to inactive in 2iL/I/F (B to A; Figures 6C and 6D). While there is enrichment of primed-specific active compartments, a previous study showed that inactive B subcompartments are largely devoid of histone modifications, including H3K27me3 and H3K9me3 (Rao et al., 2014). It is therefore likely that the primed-specific active compartments are driven by the lack of repressive modifications in 2iL/I/F hESCs (alternatively, these are 2iL/I/F-specific inactive B compartments). Additionally, cell-specific active compartments are enriched for TE expression relative to stable compartments (Figure 6E), and gene expression to a lesser extent (Figure S7F).

DISCUSSION

mESCs derived from the preimplantation blastocyst and grown in 2iL, as compared with the traditional serum and Lif, have been described as the ground state of pluripotency (Nichols and Smith, 2009; Silva and Smith, 2008). Recent gene expression studies of 2iL mESCs illustrated that their transcriptional and network analysis profiles reflect that of preimplantation blastocysts (Boroviak et al., 2014,

Figure 6. Changes in 3D Genome Architecture in 2iL/I/F hESCs

(A) Enrichment of ChIP peaks for histone marks H3K4me1, H3K27ac, H3K27me3, and H3K4me3 at overhanging TAD regions. The p value was calculated from a permutation test (N = 10,000 permutations) of randomized genomic regions with centromeres and telomeres masked.

(B) Interaction matrices of region of chr7 containing HOXA locus. Between matrices, horizontal bars with a vertical offset represent an individual TAD, 2iL/I/F in navy and primed in orange. The green bar indicates a primed boundary region >40 kb. Track of differential insulation score of 2iL/I/F versus primed cells around the HOXA locus nested in between TAD calls. ChIP-seq signal (RPKM) scaled from 0 to 20 for H3K4me1 and H3K27ac, scaled 0 to 30 for H3K27me3, 2iL/I/F in navy and primed in orange.

(C) Example of a 2iL/I/F-specific A compartment relative to primed. PC1 scale from −60 to 60.

(D) Heatmap of PC1 values at 2iL/I/F- and primed-specific A compartments. PC1 values at randomized compartments are displayed underneath. "N" and "P" denote 2iL/I/F and primed, respectively.

(E) Box plot of transposable element expression (RPKM) overlapping A to B compartment switches. "A to B" and "B to A" are 2iL/I/F to primed directions. Stable are compartments that do not switch. p values are computed using two-sample t test with one-sided alternative. ***$p < 2.2 \times 10^{-16}$.

2015). Our comparison of single-cell RNA-seq from the developing human blastocyst (Blakeley et al., 2015) to 2iL/I/F and primed hESCs demonstrated an enrichment of key developmental genes and pathways, including WNT and TGF-β, in 2iL/I/F hESCs. In addition, we described the enrichment of hundreds of 2iL/I/F-specific genes that are expressed during early embryogenesis. Coupling transcriptome data with evidence that that the genome of naive hESCs are also hypomethylated, naive versus primed hESCs can be used to model epigenomic reprogramming that occurs as cells shift between these developmental states.

The early mouse embryo undergoes dramatic chromatin remodeling. Immunofluorescence studies in mouse embryos showed that during the first few hours after fertilization, H3K4me1 levels in the paternal genome increase to match maternal levels, while histone 3 lysine 9 dimethylation (H3K9me2) is rapidly removed from the maternal genome (Lepikhov and Walter, 2004; Sarmento et al., 2004; van der Heijden et al., 2005). This is accompanied by hyperacetylation of histones prior to zygotic genome activation (Adenot et al., 1997; Wiekowski et al., 1997). The presence of H3K4 methylation inhibits interaction of DNMT3L with DNA, thus potentially contributing to the hypomethylated epigenome (Ooi et al., 2007). Based on equivalent cells in mouse, naive and primed hESCs are thought to be reflective of early human embryogenesis, capturing the preimplantation and postimplantation states, respectively (Nichols and Smith, 2009). We observe novel features of the epigenome transitioning from naive to primed. We hypothesize that widespread deposition of H3K4me1 and histone acetylation are part of the mechanism to reset the zygotic genome along with known global DNA demethylation, and that this aids to open chromatin structure for, or in response to, genome activation.

These dramatic chromatin changes during embryogenesis are likely further altered upon implantation. For example, recent ChIP-seq results for H3K27ac in the mouse embryo and serum-maintained mESCs confirmed an enrichment of H3K27ac genome-wide post-ZGA followed by a decline in mESCs (Dahl et al., 2016). Enhancer decommissioning requires LSD1 activity (Whyte et al., 2012), which is inhibited by acetylation (Forneris et al., 2005; Lee et al., 2006). Deacetylation must, therefore, precede the removal of H3K4me1 by LSD1. This stepwise decommissioning was observed as cells exited the naive state, lending support to our hypothesis that enhancer premarking is a likely component of epigenetic reprogramming during embryogenesis.

Lastly, changes in chromatin modifications are reflected in changes in 3D genome architecture. Although primed TADs are largely unchanged upon hESC differentiation (Dixon et al., 2015), most 2iL/I/F TAD boundaries are unique to this pluripotent state, subsets of which are validated by recent ChIA-PET data. Our findings suggest that TAD structures are still formalizing prior to implantation, i.e., while overall TAD architecture is in place naive boundaries are expanded or contracted relative to primed cells. This was also recently observed in the mouse embryo, where 80% of inner cell mass (ICM) TAD boundaries are also present in mESCs, as the other TADs did not reach a mESC or somatic cell-like state until later development (Du et al., 2017). We, therefore, suspect a large fraction of 2iL/I/F TADs may also be reflected in the naive human ICM. Collectively, these characteristics are likely to shape naive pluripotency and provide new insights on epigenetic reprogramming through this model of development.

EXPERIMENTAL PROCEDURES

Human Embryonic Stem Cell Culture

All human ESC culture conditions were as previously described (Sperber et al., 2015), with modifications described in Supplemental Experimental Procedures. Base media were supplemented with specific inhibitors for each growth condition.

Genome-wide Assays, Library Construction, and Sequencing

ChIP-seq was performed as previously described (Hawkins et al., 2013). Raw sequence reads were obtained from the Roadmap Epigenome Project (Hawkins et al., 2010). Replicates of aligned files were merged prior to peak calling. RNA-seq libraries, performed in duplicate, were constructed using the Scriptseq RNA-seq Library Preparation Kit. All Libraries were sequenced single-end 75 cycles on Illumina NextSeq or single-end 50 cycles on HiSeq 2500.

Computational Analysis

Details of computational analysis are provided in Supplemental Experimental Procedures. Sequencing raw reads were trimmed for low quality and adapters using TrimGalore!, and mapped to human genome (hg19) using Bowtie2 (ChIP-seq) (Langmead and Salzberg, 2012) and TopHat2 (RNA-seq) (Kim et al., 2013). Duplicates were merged. Transcript quantification was performed by Cufflinks (Trapnell et al., 2010) using GENCODE gene annotation release 19 as reference annotation. ChIP-seq peaks were called using MACS v1.4 using the –nomodel mode.

ACCESSION NUMBERS

All data are available from NCBI GEO accession number GEO: GSE90680.

SUPPLEMENTAL INFORMATION

Supplemental Information can be found online at https://doi.org/10.1016/j.stemcr.2019.04.004.

AUTHOR CONTRIBUTIONS

R.D.H. and C.B.W. conceived the study. S.L.B., C.B.W., and R.D.H. planned the study. S.L.B. and R.D.H. wrote the manuscript. S.L.B. performed ChIP-seq, RNA-seq, RRBS, analyzed ChIP-seq and RRBS data, and contributed to analyses related to RNA-seq and Hi-C. N.D.J. analyzed RNA-seq data and performed related analyses, and contributed to Hi-C analysis. R.N.A. performed Hi-C and analyzed data. J.H. performed all cell culture with guidance from C.B.W., H.R.-B., J.M., and F.N.A. contributed to ChIP-seq experiments. E.G.O. performed FACS experiments and analysis. J.A.Z. contributed to Hi-C analysis.

ACKNOWLEDGMENTS

The authors thank Dr. Gurkan Yardimci (PhD, Department of Genome Sciences, University of Washington, Seattle, WA, USA) for communication and advice on Hi-C analysis. R.D.H. is supported by funds from a John H. Tietze Award from the Tietze Foundation, the NIH/NIAMS (R01AR065952), NIH/NIDDK (R01DK103667), and the United States-Israel Binational Science Foundation (2013027). S.L.B. was supported by a Ford Foundation Fellowship Dissertation award administered by the National Academies of Sciences, Engineering, and Medicine and by the Molecular Medicine Training grant (T32GM095421). E.G.O. was supported by the Big Data for Genomics and Neuroscience training grant (T32LM012419).

Received: October 23, 2017
Revised: April 2, 2019
Accepted: April 4, 2019
Published: May 2, 2019

REFERENCES

Adenot, P.G., Mercier, Y., Renard, J.P., and Thompson, E.M. (1997). Differential H4 acetylation of paternal and maternal chromatin precedes DNA replication and differential transcriptional activity in pronuclei of 1-cell mouse embryos. Development *124*, 4615–4625.

Ahmed, K., Dehghani, H., Rugg-Gunn, P., Fussner, E., Rossant, J., and Bazett-Jones, D.P. (2010). Global chromatin architecture reflects pluripotency and lineage commitment in the early mouse embryo. PLoS One *5*, e10531.

Blakeley, P., Fogarty, N.M., del Valle, I., Wamaitha, S.E., Hu, T.X., Elder, K., Snell, P., Christie, L., Robson, P., and Niakan, K.K. (2015). Defining the three cell lineages of the human blastocyst by single-cell RNA-seq. Development *142*, 3151–3165.

Boroviak, T., Loos, R., Bertone, P., Smith, A., and Nichols, J. (2014). The ability of inner-cell-mass cells to self-renew as embryonic stem cells is acquired following epiblast specification. Nat. Cell Biol. *16*, 516–528.

Boroviak, T., Loos, R., Lombard, P., Okahara, J., Behr, R., Sasaki, E., Nichols, J., Smith, A., and Bertone, P. (2015). Lineage-specific profiling delineates the emergence and progression of naive pluripotency in mammalian embryogenesis. Dev. Cell *35*, 366–382.

Chan, Y.S., Goke, J., Ng, J.H., Lu, X., Gonzales, K.A., Tan, C.P., Tng, W.Q., Hong, Z.Z., Lim, Y.S., and Ng, H.H. (2013). Induction of a human pluripotent state with distinct regulatory circuitry that resembles preimplantation epiblast. Cell Stem Cell *13*, 663–675.

Chen, Y.-G., Li, Z., and Wang, X.-F. (2012). Where PI3K/Akt meets smads: the crosstalk determines human embryonic stem cell fate. Cell Stem Cell *10*, 231–232.

Collier, A.J., Panula, S.P., Schell, J.P., Chovanec, P., Plaza Reyes, A., Petropoulos, S., Corcoran, A.E., Walker, R., Douagi, I., Lanner, F., et al. (2017). Comprehensive cell surface protein profiling identifies specific markers of human naive and primed pluripotent states. Cell Stem Cell *20*, 874–890.e7.

Crane, E., Bian, Q., McCord, R.P., Lajoie, B.R., Wheeler, B.S., Ralston, E.J., Uzawa, S., Dekker, J., and Meyer, B.J. (2015). Condensin-driven remodelling of X chromosome topology during dosage compensation. Nature *523*, 240–244.

Creyghton, M.P., Cheng, A.W., Welstead, G.G., Kooistra, T., Carey, B.W., Steine, E.J., Hanna, J., Lodato, M.A., Frampton, G.M., Sharp, P.A., et al. (2010). Histone H3K27ac separates active from poised enhancers and predicts developmental state. Proc. Natl. Acad. Sci. U S A *107*, 21931–21936.

Dahl, J.A., Jung, I., Aanes, H., Greggains, G.D., Manaf, A., Lerdrup, M., Li, G., Kuan, S., Li, B., Lee, A.Y., et al. (2016). Broad histone H3K4me3 domains in mouse oocytes modulate maternal-to-zygotic transition. Nature *537*, 548–552.

Deng, X., Ma, W., Ramani, V., Hill, A., Yang, F., Ay, F., Berletch, J.B., Blau, C.A., Shendure, J., Duan, Z., et al. (2015). Bipartite structure of the inactive mouse X chromosome. Genome Biol. *16*, 152.

Dixon, J.R., Selvaraj, S., Yue, F., Kim, A., Li, Y., Shen, Y., Hu, M., Liu, J.S., and Ren, B. (2012). Topological domains in mammalian genomes identified by analysis of chromatin interactions. Nature *485*, 376–380.

Dixon, J.R., Jung, I., Selvaraj, S., Shen, Y., Antosiewicz-Bourget, J.E., Lee, A.Y., Ye, Z., Kim, A., Rajagopal, N., Xie, W., et al. (2015). Chromatin architecture reorganization during stem cell differentiation. Nature *518*, 331–336.

Du, Z., Zheng, H., Huang, B., Ma, R., Wu, J., Zhang, X., He, J., Xiang, Y., Wang, Q., Li, Y., et al. (2017). Allelic reprogramming of 3D chromatin architecture during early mammalian development. Nature *547*, 232–235.

ENCODE Project Consortium (2012). An integrated encyclopedia of DNA elements in the human genome. Nature *489*, 57–74.

Forneris, F., Binda, C., Vanoni, M.A., Battaglioli, E., and Mattevi, A. (2005). Human histone demethylase LSD1 reads the histone code. J. Biol. Chem. *280*, 41360–41365.

Gafni, O., Weinberger, L., Mansour, A.A., Manor, Y.S., Chomsky, E., Ben-Yosef, D., Kalma, Y., Viukov, S., Maza, I., Zviran, A., et al. (2013). Derivation of novel human ground state naive pluripotent stem cells. Nature *504*, 282–286.

Giorgetti, L., Lajoie, B.R., Carter, A.C., Attia, M., Zhan, Y., Xu, J., Chen, C.J., Kaplan, N., Chang, H.Y., Heard, E., et al. (2016). Structural organization of the inactive X chromosome in the mouse. Nature *535*, 575–579.

Guo, H., Zhu, P., Yan, L., Li, R., Hu, B., Lian, Y., Yan, J., Ren, X., Lin, S., Li, J., et al. (2014). The DNA methylation landscape of human early embryos. Nature *511*, 606–610.

Guo, G., von Meyenn, F., Santos, F., Chen, Y., Reik, W., Bertone, P., Smith, A., and Nichols, J. (2016). Naive pluripotent stem cells derived directly from isolated cells of the human inner cell mass. Stem Cell Reports *6*, 437–446.

Hanna, J., Cheng, A.W., Saha, K., Kim, J., Lengner, C.J., Soldner, F., Cassady, J.P., Muffat, J., Carey, B.W., and Jaenisch, R. (2010). Human embryonic stem cells with biological and epigenetic characteristics similar to those of mouse ESCs. Proc. Natl. Acad. Sci. U S A *107*, 9222–9227.

Hawkins, R.D., Hon, G.C., Lee, L.K., Ngo, Q., Lister, R., Pelizzola, M., Edsall, L.E., Kuan, S., Luu, Y., Klugman, S., et al. (2010). Distinct epigenomic landscapes of pluripotent and lineage-committed human cells. Cell Stem Cell *6*, 479–491.

Hawkins, R.D., Hon, G.C., Yang, C., Antosiewicz-Bourget, J.E., Lee, L.K., Ngo, Q.M., Klugman, S., Ching, K.A., Edsall, L.E., Ye, Z., et al. (2011). Dynamic chromatin states in human ES cells reveal potential regulatory sequences and genes involved in pluripotency. Cell Res. *21*, 1393–1409.

Hawkins, R.D., Larjo, A., Tripathi, S.K., Wagner, U., Luu, Y., Lonnberg, T., Raghav, S.K., Lee, L.K., Lund, R., Ren, B., et al. (2013). Global chromatin state analysis reveals lineage-specific enhancers during the initiation of human T helper 1 and T helper 2 cell polarization. Immunity *38*, 1271–1284.

Heintzman, N.D., Stuart, R.K., Hon, G., Fu, Y., Ching, C.W., Hawkins, R.D., Barrera, L.O., Van Calcar, S., Qu, C., Ching, K.A., et al. (2007). Distinct and predictive chromatin signatures of transcriptional promoters and enhancers in the human genome. Nat. Genet. *39*, 311–318.

Heintzman, N.D., Hon, G.C., Hawkins, R.D., Kheradpour, P., Stark, A., Harp, L.F., Ye, Z., Lee, L.K., Stuart, R.K., Ching, C.W., et al. (2009). Histone modifications at human enhancers reflect global cell-type-specific gene expression. Nature *459*, 108–112.

Ji, X., Dadon, D.B., Powell, B.E., Fan, Z.P., Borges-Rivera, D., Shachar, S., Weintraub, A.S., Hnisz, D., Pegoraro, G., Lee, T.I., et al. (2016). 3D chromosome regulatory landscape of human pluripotent cells. Cell Stem Cell *18*, 262–275.

Kim, D., Pertea, G., Trapnell, C., Pimentel, H., Kelley, R., and Salzberg, S.L. (2013). TopHat2: accurate alignment of transcriptomes in the presence of insertions, deletions and gene fusions. Genome Biol. *14*, R36.

Langmead, B., and Salzberg, S.L. (2012). Fast gapped-read alignment with Bowtie 2. Nat. Methods *9*, 357–359.

Lee, M.G., Wynder, C., Bochar, D.A., Hakimi, M.A., Cooch, N., and Shiekhattar, R. (2006). Functional interplay between histone demethylase and deacetylase enzymes. Mol. Cell. Biol. *26*, 6395–6402.

Lepikhov, K., and Walter, J. (2004). Differential dynamics of histone H3 methylation at positions K4 and K9 in the mouse zygote. BMC Dev. Biol. *4*, 12.

Lieberman-Aiden, E., van Berkum, N.L., Williams, L., Imakaev, M., Ragoczy, T., Telling, A., Amit, I., Lajoie, B.R., Sabo, P.J., Dorschner, M.O., et al. (2009). Comprehensive mapping of long-range interactions reveals folding principles of the human genome. Science *326*, 289–293.

Liu, H., Kim, J.M., and Aoki, F. (2004). Regulation of histone H3 lysine 9 methylation in oocytes and early pre-implantation embryos. Development *131*, 2269–2280.

Meshorer, E., Yellajoshula, D., George, E., Scambler, P.J., Brown, D.T., and Misteli, T. (2006). Hyperdynamic plasticity of chromatin proteins in pluripotent embryonic stem cells. Dev. Cell *10*, 105–116.

Moody, J.D., Levy, S., Mathieu, J., Xing, Y., Kim, W., Dong, C., Tempel, W., Robitaille, A.M., Dang, L.T., Ferreccio, A., et al. (2017). First critical repressive H3K27me3 marks in embryonic stem cells identified using designed protein inhibitor. Proc. Natl. Acad. Sci. U S A *114*, 10125–10130.

Niakan, K.K., and Eggan, K. (2013). Analysis of human embryos from zygote to blastocyst reveals distinct gene expression patterns relative to the mouse. Dev. Biol. *375*, 54–64.

Nichols, J., and Smith, A. (2009). Naive and primed pluripotent states. Cell Stem Cell *4*, 487–492.

Ooi, S.K., Qiu, C., Bernstein, E., Li, K., Jia, D., Yang, Z., Erdjument-Bromage, H., Tempst, P., Lin, S.P., Allis, C.D., et al. (2007). DNMT3L connects unmethylated lysine 4 of histone H3 to de novo methylation of DNA. Nature *448*, 714–717.

Parker, S.C., Stitzel, M.L., Taylor, D.L., Orozco, J.M., Erdos, M.R., Akiyama, J.A., van Bueren, K.L., Chines, P.S., Narisu, N., Black, B.L., et al. (2013). Chromatin stretch enhancer states drive cell-specific gene regulation and harbor human disease risk variants. Proc. Natl. Acad. Sci. U S A *110*, 17921–17926.

Rada-Iglesias, A., Bajpai, R., Swigut, T., Brugmann, S.A., Flynn, R.A., and Wysocka, J. (2011). A unique chromatin signature uncovers early developmental enhancers in humans. Nature *470*, 279–283.

Rao, S.S., Huntley, M.H., Durand, N.C., Stamenova, E.K., Bochkov, I.D., Robinson, J.T., Sanborn, A.L., Machol, I., Omer, A.D., Lander, E.S., et al. (2014). A 3D map of the human genome at kilobase resolution reveals principles of chromatin looping. Cell *159*, 1665–1680.

Rossant, J. (2015). Mouse and human blastocyst-derived stem cells: vive les differences. Development *142*, 9–12.

Sarmento, O.F., Digilio, L.C., Wang, Y., Perlin, J., Herr, J.C., Allis, C.D., and Coonrod, S.A. (2004). Dynamic alterations of specific histone modifications during early murine development. J. Cell Sci. *117*, 4449–4459.

Shin, H., Shi, Y., Dai, C., Tjong, H., Gong, K., Alber, F., and Zhou, X.J. (2016). TopDom: an efficient and deterministic method for identifying topological domains in genomes. Nucleic Acids Res. *44*, e70.

Silva, J., and Smith, A. (2008). Capturing pluripotency. Cell *132*, 532–536.

Sperber, H., Mathieu, J., Wang, Y., Ferreccio, A., Hesson, J., Xu, Z., Fischer, K.A., Devi, A., Detraux, D., Gu, H., et al. (2015). The metabolome regulates the epigenetic landscape during naive-to-primed human embryonic stem cell transition. Nat. Cell Biol. *17*, 1523–1535.

Takashima, Y., Guo, G., Loos, R., Nichols, J., Ficz, G., Krueger, F., Oxley, D., Santos, F., Clarke, J., Mansfield, W., et al. (2014). Resetting transcription factor control circuitry toward ground-state pluripotency in human. Cell *158*, 1254–1269.

Theunissen, T.W., Powell, B.E., Wang, H., Mitalipova, M., Faddah, D.A., Reddy, J., Fan, Z.P., Maetzel, D., Ganz, K., Shi, L., et al. (2014). Systematic identification of culture conditions for induction and maintenance of naive human pluripotency. Cell Stem Cell *15*, 471–487.

Theunissen, T.W., Friedli, M., He, Y., Planet, E., O'Neil, R.C., Markoulaki, S., Pontis, J., Wang, H., Iouranova, A., Imbeault, M., et al. (2016). Molecular criteria for defining the naive human pluripotent state. Cell Stem Cell *19*, 502–515.

Trapnell, C., Williams, B.A., Pertea, G., Mortazavi, A., Kwan, G., van Baren, M.J., Salzberg, S.L., Wold, B.J., and Pachter, L. (2010). Transcript assembly and quantification by RNA-Seq reveals unannotated transcripts and isoform switching during cell differentiation. Nat. Biotechnol. *28*, 511–515.

Valamehr, B., Robinson, M., Abujarour, R., Rezner, B., Vranceanu, F., Le, T., Medcalf, A., Lee, T.T., Fitch, M., Robbins, D., et al. (2014). Platform for induction and maintenance of transgene-free hiPSCs resembling ground state pluripotent stem cells. Stem Cell Reports *2*, 366–381.

van der Heijden, G.W., Dieker, J.W., Derijck, A.A., Muller, S., Berden, J.H., Braat, D.D., van der Vlag, J., and de Boer, P. (2005). Asymmetry in histone H3 variants and lysine methylation between paternal and maternal chromatin of the early mouse zygote. Mech. Dev. *122*, 1008–1022.

Ware, C.B. (2016). Concise review: lessons from naïve human pluripotent cells. Stem Cells *35*, 35–41.

Ware, C.B., Nelson, A.M., Mecham, B., Hesson, J., Zhou, W., Jonlin, E.C., Jimenez-Caliani, A.J., Deng, X., Cavanaugh, C., Cook, S., et al. (2014). Derivation of naive human embryonic stem cells. Proc. Natl. Acad. Sci. U S A *111*, 4484–4489.

Whyte, W.A., Bilodeau, S., Orlando, D.A., Hoke, H.A., Frampton, G.M., Foster, C.T., Cowley, S.M., and Young, R.A. (2012). Enhancer decommissioning by LSD1 during embryonic stem cell differentiation. Nature *482*, 221–225.

Whyte, W.A., Orlando, D.A., Hnisz, D., Abraham, B.J., Lin, C.Y., Kagey, M.H., Rahl, P.B., Lee, T.I., and Young, R.A. (2013). Master transcription factors and mediator establish super-enhancers at key cell identity genes. Cell *153*, 307–319.

Wiekowski, M., Miranda, M., Nothias, J.Y., and DePamphilis, M.L. (1997). Changes in histone synthesis and modification at the beginning of mouse development correlate with the establishment of chromatin mediated repression of transcription. J. Cell Sci. *110* (Pt 10), 1147–1158.

Wu, J., and Izpisua Belmonte, J.C. (2015). Dynamic pluripotent stem cell states and their applications. Cell Stem Cell *17*, 509–525.

Yan, L., Yang, M., Guo, H., Yang, L., Wu, J., Li, R., Liu, P., Lian, Y., Zheng, X., Yan, J., et al. (2013). Single-cell RNA-Seq profiling of human preimplantation embryos and embryonic stem cells. Nat. Struct. Mol. Biol. *20*, 1131–1139.

Zhang, H.M., Liu, T., Liu, C.J., Song, S., Zhang, X., Liu, W., Jia, H., Xue, Y., and Guo, A.Y. (2015). AnimalTFDB 2.0: a resource for expression, prediction and functional study of animal transcription factors. Nucleic Acids Res. *43*, D76–D81.

Zhou, W., Choi, M., Margineantu, D., Margaretha, L., Hesson, J., Cavanaugh, C., Blau, C.A., Horwitz, M.S., Hockenbery, D., Ware, C., et al. (2012). HIF1alpha induced switch from bivalent to exclusively glycolytic metabolism during ESC-to-EpiSC/hESC transition. EMBO J. *31*, 2103–2116.

Zimmerlin, L., Park, T.S., and Zambidis, E.T. (2017). Capturing human naive pluripotency in the embryo and in the dish. Stem Cells Dev. *26*, 1141–1161.

Stem Cell Reports, Volume *12*

Supplemental Information

Enhancer Chromatin and 3D Genome Architecture Changes from Naive to Primed Human Embryonic Stem Cell States

Stephanie L. Battle, Naresh Doni Jayavelu, Robert N. Azad, Jennifer Hesson, Faria N. Ahmed, Eliah G. Overbey, Joseph A. Zoller, Julie Mathieu, Hannele Ruohola-Baker, Carol B. Ware, and R. David Hawkins

SUPPLEMENTAL INFORMATION

Enhancer chromatin and 3D genome architecture changes from naïve to primed human embryonic stem cell states

Stephanie L. Battle[1,2], Naresh Doni Jayavelu[1,2,3,6], Robert N. Azad[1,2,6], Jennifer Hesson[2,4], Faria N. Ahmed[1,2], Eliah G. Overbey[1,2], Joseph A. Zoller[1], Julie Mathieu[2,5], Hannele Ruohola-Baker[2,5], Carol B. Ware[2,4], R. David Hawkins[1,2,3,*]

Figure S1

A

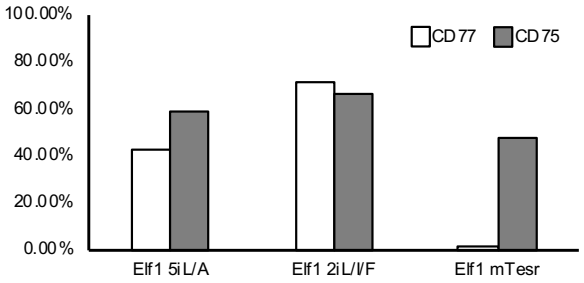

B

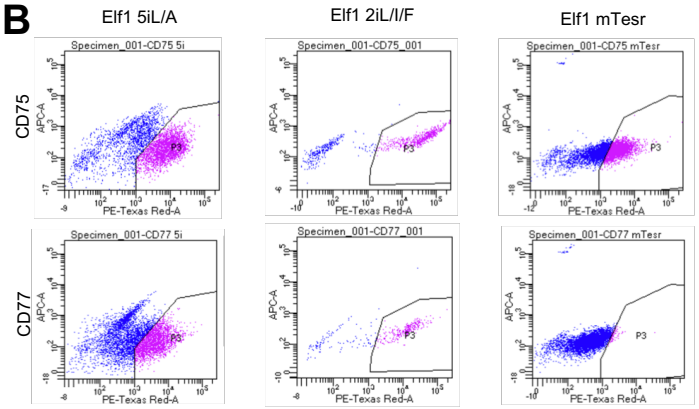

C

Average CpG Methylation Levels

Growth Condition	# CpGs	Coverage cutoff	Avg Meth level
Elf1 5iL/A	2,678,704	10x	14%
Elf1 2iL/I/F	2,847,041	10x	30%
Elf1 AF	2,533,524	10x	27%
H9	1,552,396	10x	53%

G

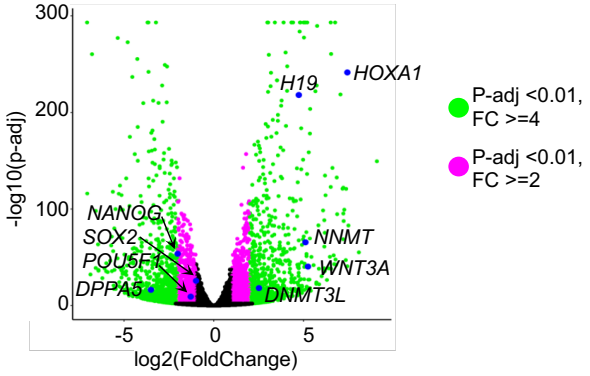

TR Up	2iL/I/F Up
995	883
2,037	1,920

H

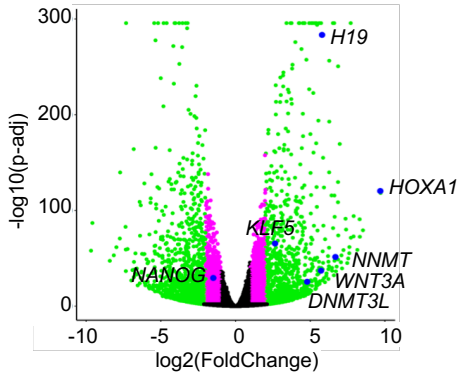

Primed Up	2iL/I/F Up
1,505	1,184
2,993	2,431

D

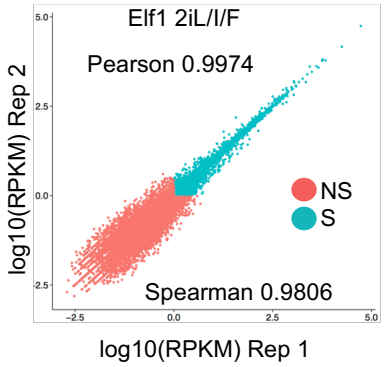

E

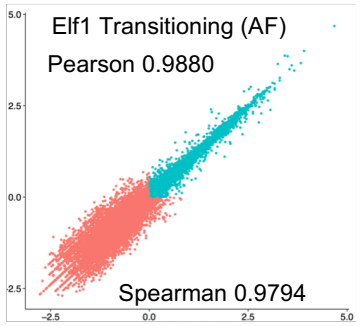

F

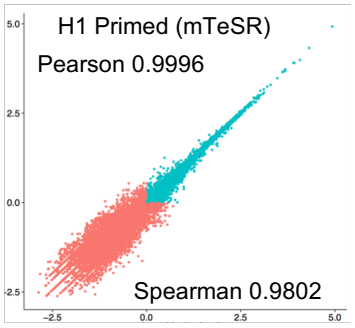

I DEGs Pathways 2iL/I/F : TR

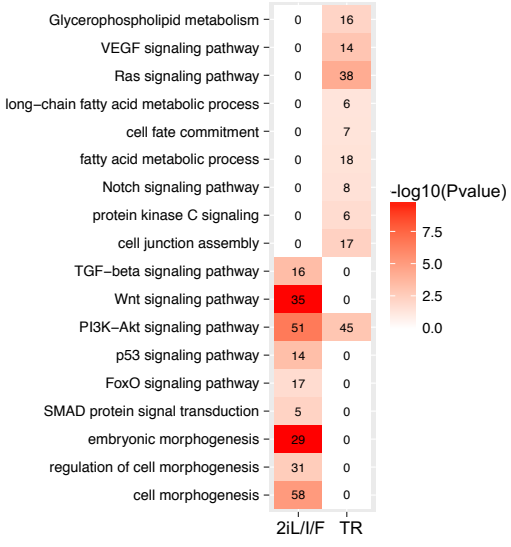

J DEGs Pathways 2iL/I/F : Primed

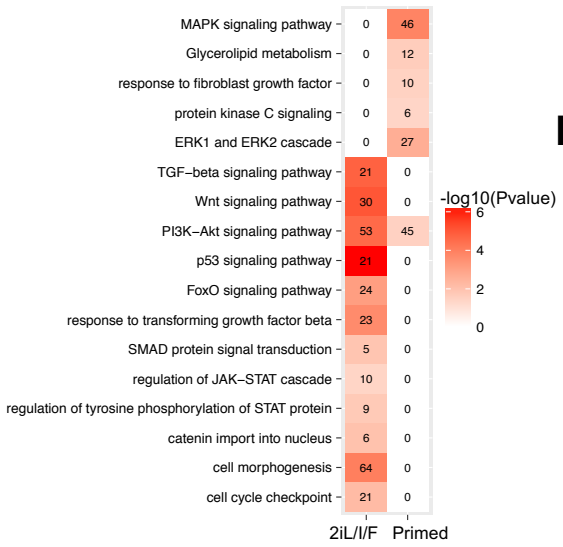

Figure S1: RNA-seq replicates and DEGs in Key Pathways
(A) Graph of percent of Elf1 5iL/A, 2iL/I/F, and mTesr (primed) hESCs positive for naïve cell surface markers as determined by Collier et al., 2017. (B) FACS scatterplots after gating for single cells, the P3 population was counted as positive for either CD75 or CD77. (C) Table shows average CpG DNA methylation levels as determined by RRBS. H9 data were taken from Kyttala et al., 2016. (D-F) Correlation between RNA-seq replicates, log10(RPKM) is plotted. On figure "NS" means not significant and "S" means significant. (G-H) Volcano plot of differentially expressed genes (DEGs) in 2iL/I/F versus transitioning (G) and 2iL/I/F versus primed (H) pairwise comparison. Genes in magenta have P-adj < 0.01 and fold change ≥ 2 while genes in green have P-adj < 0.01 and fold change ≥ 4. (I-J) Heatmap showing significantly overrepresented GO terms and KEGG pathways based on DEGs in 2iL/I/F versus transitioning and 2iL/I/F versus primed pairwise comparison.

Figure S2

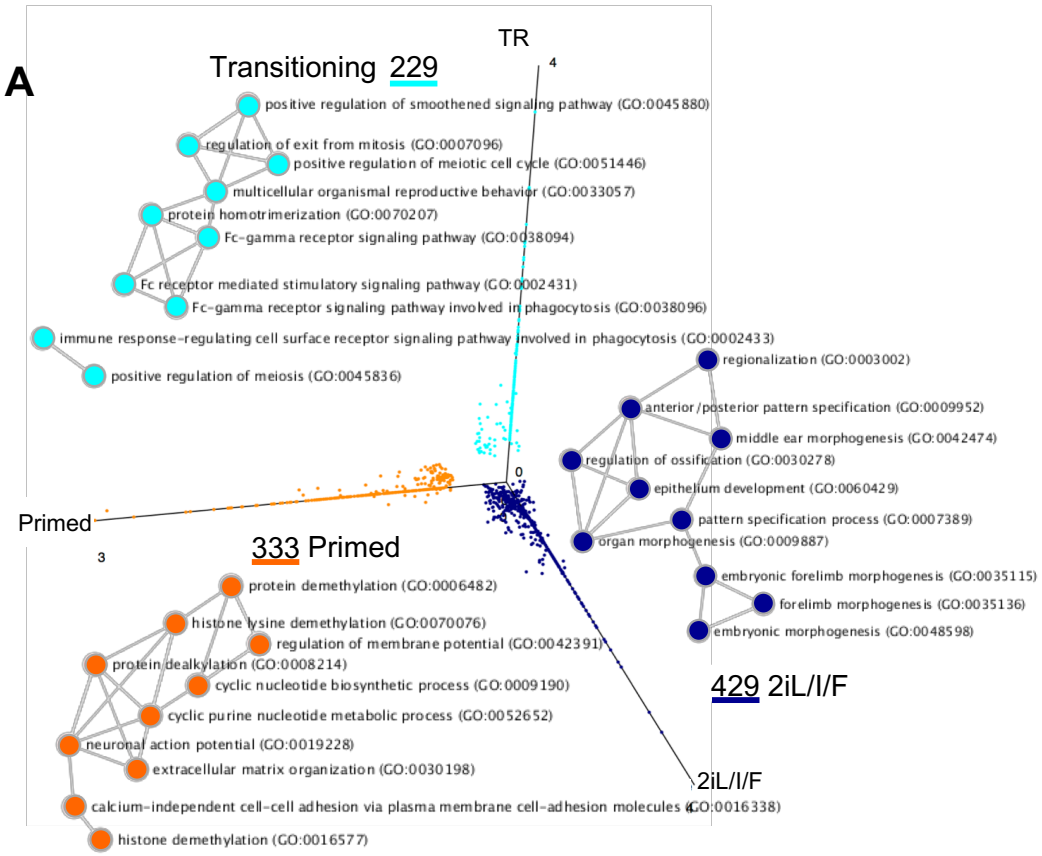
A
TR
Transitioning 229
positive regulation of smoothened signaling pathway (GO:0045880)
regulation of exit from mitosis (GO:0007096)
positive regulation of meiotic cell cycle (GO:0051446)
multicellular organismal reproductive behavior (GO:0033057)
protein homotrimerization (GO:0070207)
Fc-gamma receptor signaling pathway (GO:0038094)
Fc receptor mediated stimulatory signaling pathway (GO:0002431)
Fc-gamma receptor signaling pathway involved in phagocytosis (GO:0038096)
immune response-regulating cell surface receptor signaling pathway involved in phagocytosis (GO:0002433)
positive regulation of meiosis (GO:0045836)
regionalization (GO:0003002)
anterior/posterior pattern specification (GO:0009952)
middle ear morphogenesis (GO:0042474)
regulation of ossification (GO:0030278)
epithelium development (GO:0060429)
pattern specification process (GO:0007389)
organ morphogenesis (GO:0009887)
embryonic forelimb morphogenesis (GO:0035115)
forelimb morphogenesis (GO:0035136)
embryonic morphogenesis (GO:0048598)
Primed
333 Primed
protein demethylation (GO:0006482)
histone lysine demethylation (GO:0070076)
regulation of membrane potential (GO:0042391)
protein dealkylation (GO:0008214)
cyclic nucleotide biosynthetic process (GO:0009190)
cyclic purine nucleotide metabolic process (GO:0052652)
neuronal action potential (GO:0019228)
extracellular matrix organization (GO:0030198)
calcium-independent cell-cell adhesion via plasma membrane cell-adhesion molecules (GO:0016338)
histone demethylation (GO:0016577)
429 2iL/I/F
2iL/I/F
4
3
0

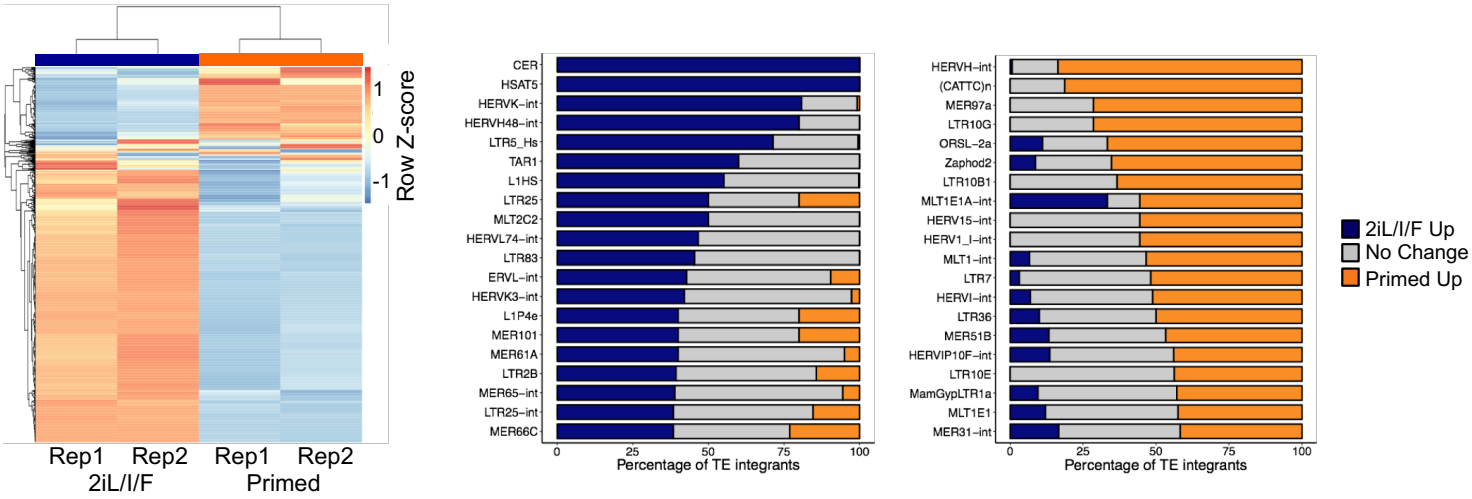
B
TE Signature in 2iL/I/F and Primed
Row Z-score
1
0
-1
Rep1
Rep2
Rep1
Rep2
2iL/I/F
Primed
CER
HSAT5
HERVK-int
HERVH48-int
LTR5_Hs
TAR1
L1HS
LTR25
MLT2C2
HERVL74-int
LTR83
ERVL-int
HERVK3-int
L1P4e
MER101
MER61A
LTR2B
MER65-int
LTR25-int
MER66C
0
25
50
75
100
Percentage of TE integrants
HERVH-int
(CATTC)n
MER97a
LTR10G
ORSL-2a
Zaphod2
LTR10B1
MLT1E1A-int
HERV15-int
HERV1_I-int
MLT1-int
LTR7
HERVI-int
LTR36
MER51B
HERVIP10F-int
LTR10E
MamGypLTR1a
MLT1E1
MER31-int
0
25
50
75
100
Percentage of TE integrants
2iL/I/F Up
No Change
Primed Up

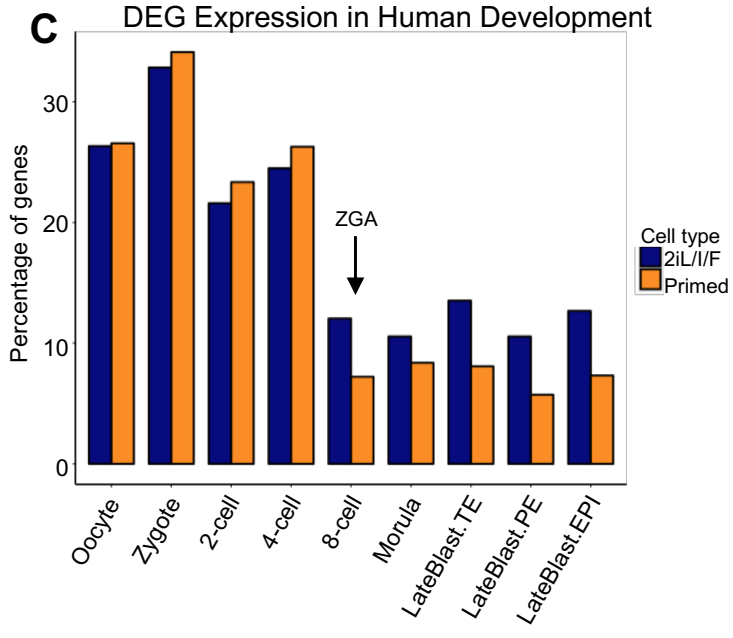
C
DEG Expression in Human Development
Percentage of genes
30
20
10
0
ZGA
Cell type
2iL/I/F
Primed
Oocyte
Zygote
2-cell
4-cell
8-cell
Morula
LateBlast.TE
LateBlast.PE
LateBlast.EPI

Figure S2: Cell-type Specific Genes and Transposable Elements
(A) Cell type-specific genes in the different hESC stages by applying a cutoff of a RPKM value greater than or equal to two in one cell type and less than one in the other two cell types. GO terms shown in network, connected by shared genes between terms. (B) Hierarchical clustering of transposable elements expression separates 2iL/I/F from primed hESCs in first panel. Second and third panel show the percentage of integrants that are upregulated in each cell type. (C) Percentage of genes upregulated in pairwise comparison of 2iL/I/F or primed hESCs that are also found to be upregulated in human embryo developmental stages.

Figure S3

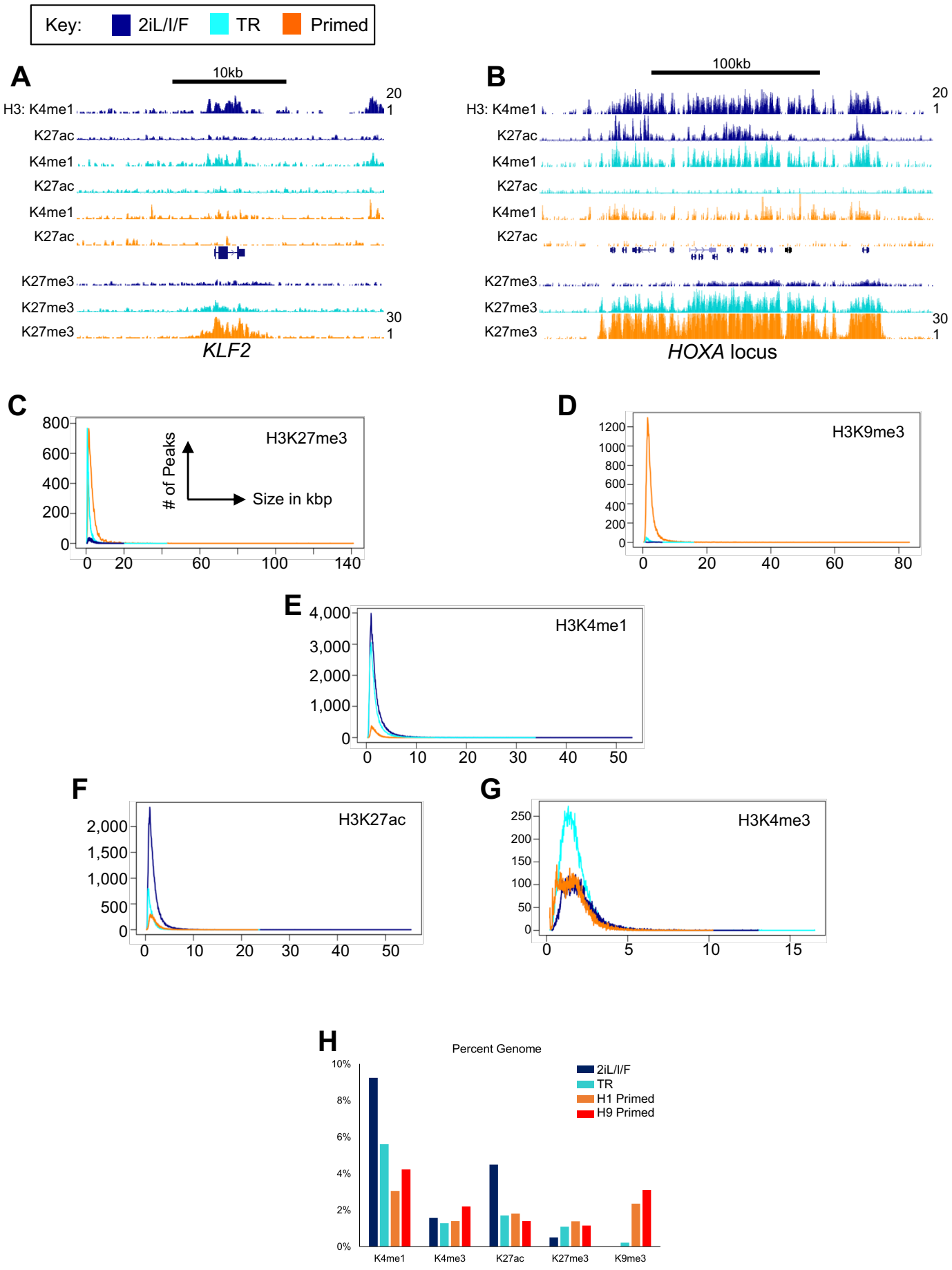
Key: 2iL/I/F TR Primed
A
10kb
H3: K4me1
K27ac
K4me1
K27ac
K4me1
K27ac
K27me3
K27me3
K27me3
20
1
30
1
KLF2
B
100kb
H3: K4me1
K27ac
K4me1
K27ac
K4me1
K27ac
K27me3
K27me3
K27me3
20
1
30
1
HOXA locus
C
H3K27me3
# of Peaks
Size in kbp
800
600
400
200
0
0 20 60 100 140
D
H3K9me3
1200
1000
800
600
400
200
0
0 20 40 60 80
E
H3K4me1
4,000
3,000
2,000
1,000
0
0 10 20 30 40 50
F
H3K27ac
2,000
1,500
1,000
500
0
0 10 20 30 40 50
G
H3K4me3
250
200
150
100
50
0
0 5 10 15
H
Percent Genome
2iL/I/F
TR
H1 Primed
H9 Primed
10%
8%
6%
4%
2%
0%
K4me1 K4me3 K27ac K27me3 K9me3

Figure S3: Histone Modifications globally and Chromosome X
(A-B) UCSC Browser image of the *KLF2* (A) and *HOXA* (B) loci. H3K4me1 and H3K27ac (top 6 tracks, RPKM scale 1-20) and H3K27me3 (bottom 3 tracks, RPKM scale 1-30) are shown for 2iL/I/F, transitioning and primed ChIP-seq data. (C-G) Histograms showing distribution of peak lengths for (C) H3K27me3, (D) H3K9me3, (E) H3K4me1, (F) H3K27ac and (G) H3K4me3. (H) Percent of human genome bases covered by histone modifications in primed cell line H9. H9 ChIP-seq data taken from the Roadmap Project.

Figure S4

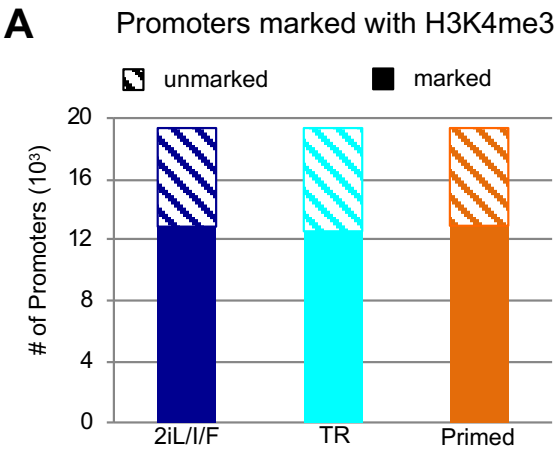
A
Promoters marked with H3K4me3
unmarked
marked
# of Promoters (10³)
20
16
12
8
4
0
2iL/I/F
TR
Primed

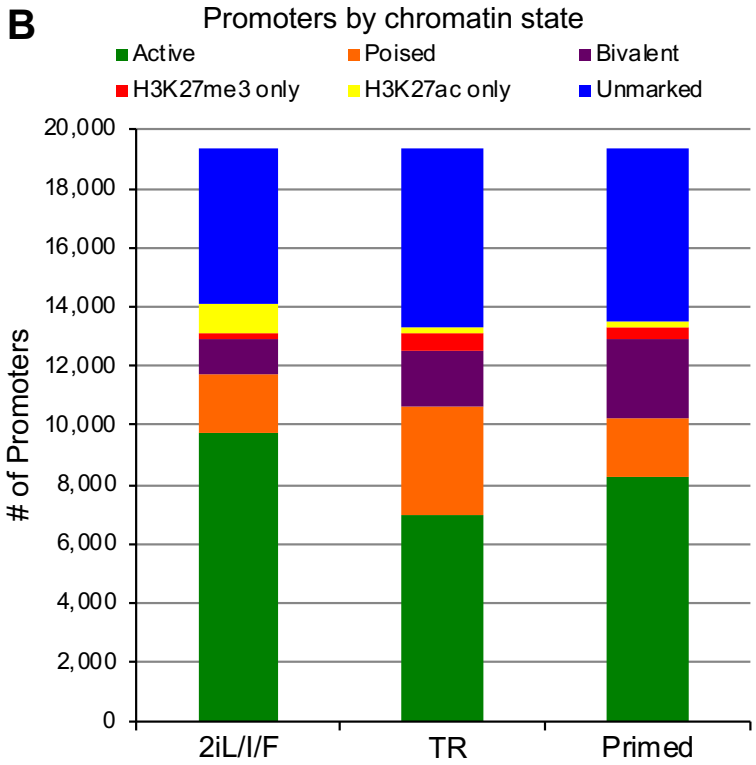
B
Promoters by chromatin state
Active
Poised
Bivalent
H3K27me3 only
H3K27ac only
Unmarked
# of Promoters
20,000
18,000
16,000
14,000
12,000
10,000
8,000
6,000
4,000
2,000
0
2iL/I/F
TR
Primed

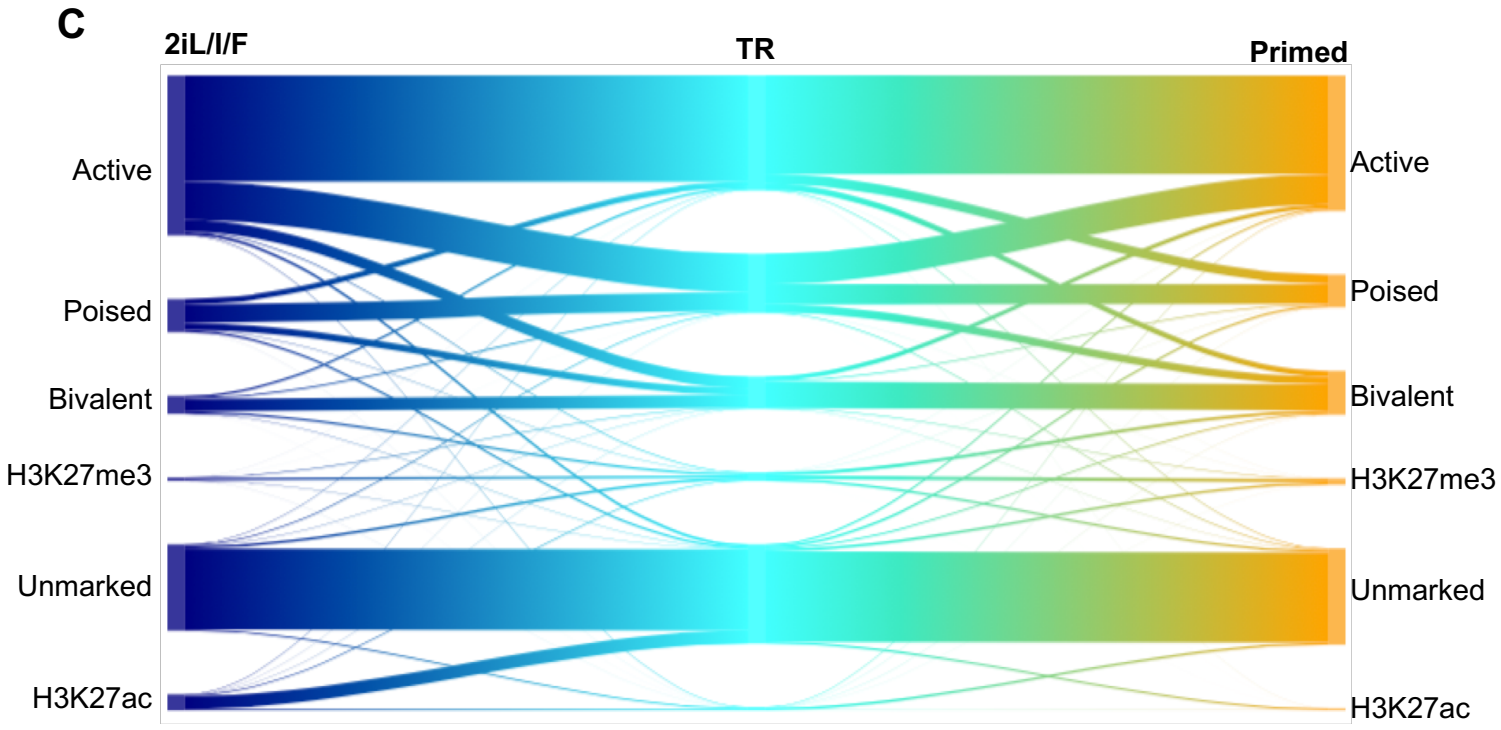
C
2iL/I/F
TR
Primed
Active
Poised
Bivalent
H3K27me3
Unmarked
H3K27ac
Active
Poised
Bivalent
H3K27me3
Unmarked
H3K27ac

Figure S4: Histone Modifications at Promoters and Bivalent Gene Ontology
(A) Number of GENCODE coding gene promoters marked with H3K4me3 or unmarked in each hESC stage. (B) Breakdown of promoter chromatin state categories. Graph shows how many gene promoters are found in each category. (C) Sankey plot of all promoter state transitions between three hES cell types.

Figure S5

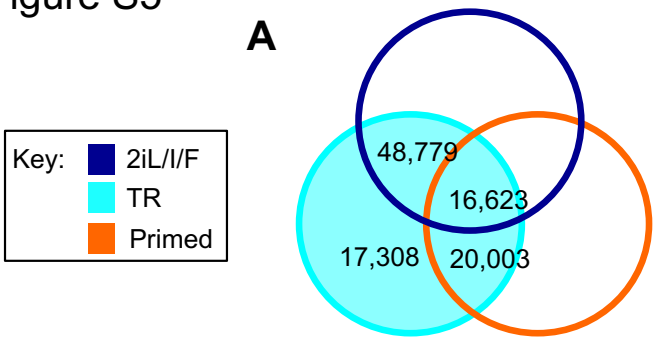

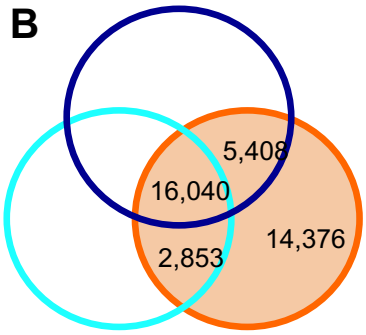

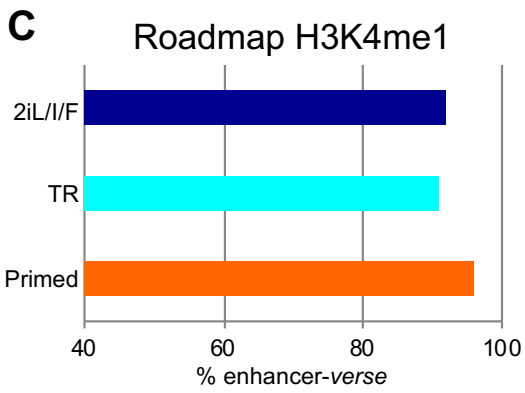

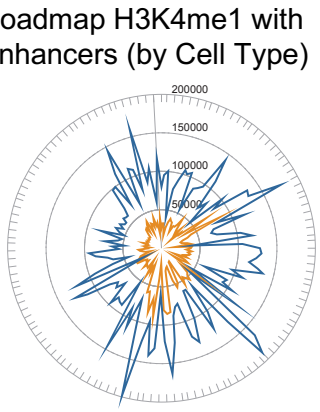

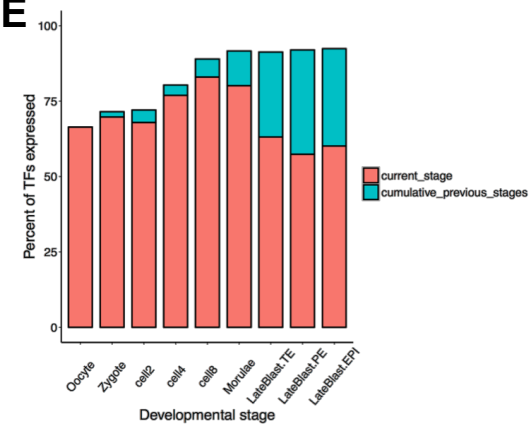

F

Enhancer Class	2iL/I/F	TR	Primed
Active H3K4me1 + H3K27ac	31,673	7,990	8,946
Poised H3K4me1 only	65,334	58,497	28,067
Poised H3K4me1 + H3K27me3	1,013	2,980	1,664

G

	H3K4me1				H3K27ac				H3K4me3
	< 5 kb	≥ 5 kb	≥ 10 kb	≥ 20 kb	< 5 kb	≥ 5 kb	≥ 10 kb	≥ 20 kb	≥ 5 kb
	Short	**Broad**	**Grande**	**Venti**	**Short**	**Broad**	**Grande**	**Venti**	**Broad**
2iL/I/F	109,587	7,412	1,413	157	65,170	2,330	294	20	283
TR	80,818	3,122	391	18	36,460	241	10	1	74
Primed	46,472	371	10	0	23,865	803	53	3	144

H

2iL/I/F	8,140	6,610	7,428
TR	7,383	5,153	6,559
Primed	6,123	5,249	6,700

I

	2iL/I/F	TR	Primed
Broad K4me1 w/ K27ac	87.72%	49.01%	71.16%
Broad K4me1 w/ Broad K27ac	23.46%	4.13%	22.64%
Broad K27ac w/ Broad K4me1	78.58%	52.70%	10.46%

Figure S5: Characteristics of Enhancers in hESCs
(A-B) Venn diagrams of enhancer overlaps for transitioning (A) and primed (B) cells with other cell types. Venns are separate because one peak in one cell type can overlap multiple peaks in another cell type. (C) Percent of hESC H3K4me1 genomic space (% bases or enhancer-verse) occupied by Roadmap H3K4me1 from 127 cell types. (D) Number of Roadmap H3K4me1 peaks from 127 cell types overlapping with 2iL/I/F and primed H3K4me1 enhancers. (E) Percent of transcription factors, annotated from Animal TFDB, expressed at each stage of embryogenesis and cumulatively across stages using single cell RNA-seq data from Yan et al. (Yan et al., 2013). (F) Number of enhancers peaks that fall into the category of active, poised HK4me1 only or poised H3K27me3 enhancer classes. (G) Number of H3K4me1, H3K27ac and H3K4me3 peaks, broken down by size. (H) Average length of broad (≥ 5 kb) H3K4me1 and H3K27ac domains and the average number of bases overlapped in shared regions. (I) Percent of broad peaks that overlap in these comparisons: broad H3K4me1 with any H3K27ac overlap, broad H3K4me1 with only broad H3K27ac overlap, or broad H3K27ac with broad H3K4me1 overlap.

Figure S6

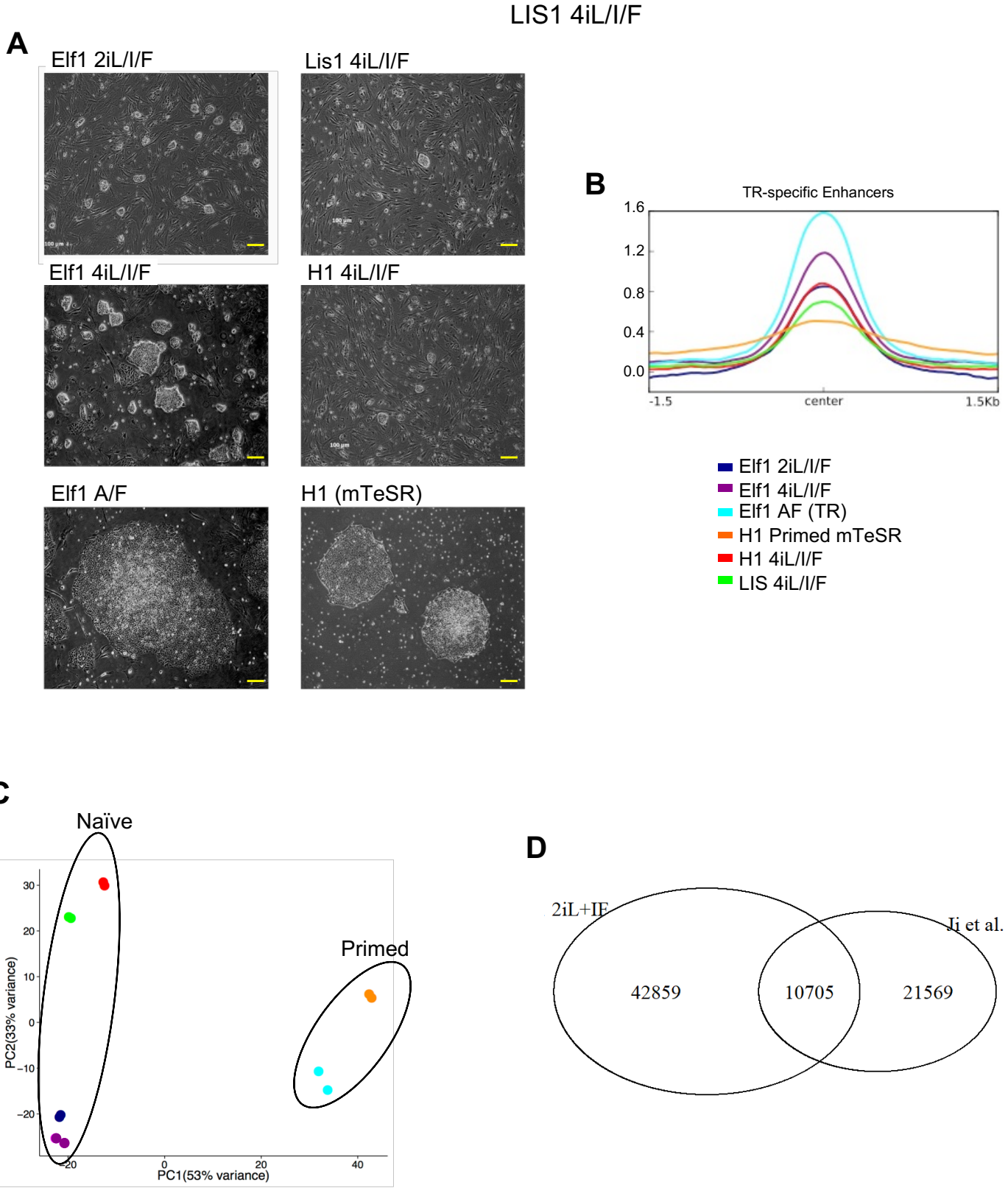
LIS1 4iL/I/F
A
Elf1 2iL/I/F
Lis1 4iL/I/F
Elf1 4iL/I/F
H1 4iL/I/F
Elf1 A/F
H1 (mTeSR)
B
TR-specific Enhancers
1.6
1.2
0.8
0.4
0.0
-1.5
center
1.5Kb
Elf1 2iL/I/F
Elf1 4iL/I/F
Elf1 AF (TR)
H1 Primed mTeSR
H1 4iL/I/F
LIS 4iL/I/F
C
Naïve
Primed
PC2(33% variance)
PC1(53% variance)
D
2iL+IF
Ji et al.
42859
10705
21569

Figure S6: RNA-seq and ChIP-seq of hESCs in Different Growth Conditions
(A) Representative images of cell lines in each growth condition used for this study. Yellow bar is 200um. (B) Average normalized ChIP-seq signal in all naïve and primed hESCs at transitioning-specific enhancers. (C) PCA of autosomal gene expression, naïve cells cluster separately from primed cells. (D) Venn diagram showing the number of Elf1 2iL/I/F H3K27ac peaks that overlap 5iL/A H3K27ac peak calls from Ji et al., 2016.

Figure S7

A

Hi-C library	Raw read pairs	Processed read pairs	Cis interactions	Cis interactions within 20 kb
Elf1 Replicate 1	798,771,830	318,226,786	224,980,721	65,753,953
Elf1 Replicate 2	770,256,147	324,524,006	221,137,452	62,491,765
H1 Replicate 1	237,662,270	35,822,152	19,713,347	3,369,816
H1 Replicate 2	496,522,946	160,344,628	124,240,997	20,935,372

B

Feature	2iL/I/F	Primed
TAD	6,119	5,822
Boundary	5,487	5,279
Boundary > 40 kb	433	351

C

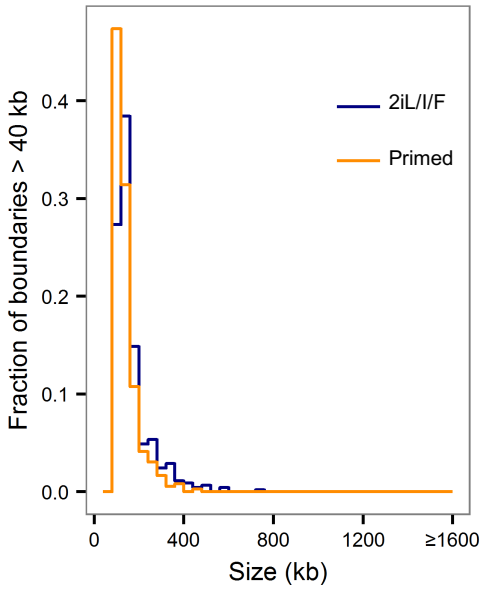

D

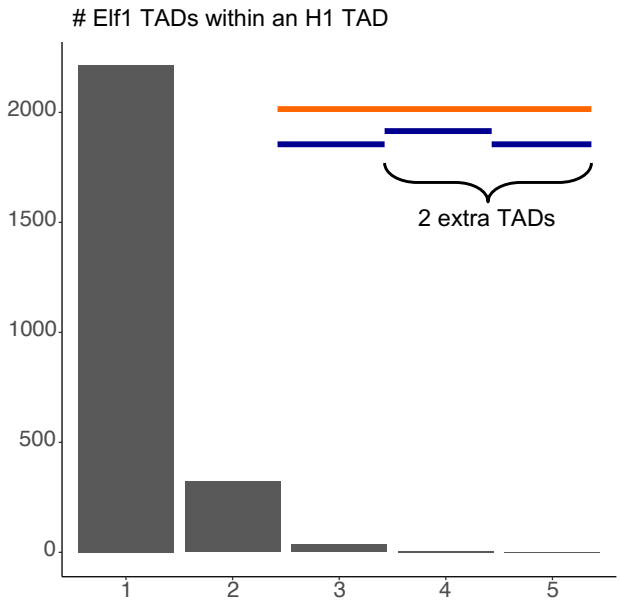

E

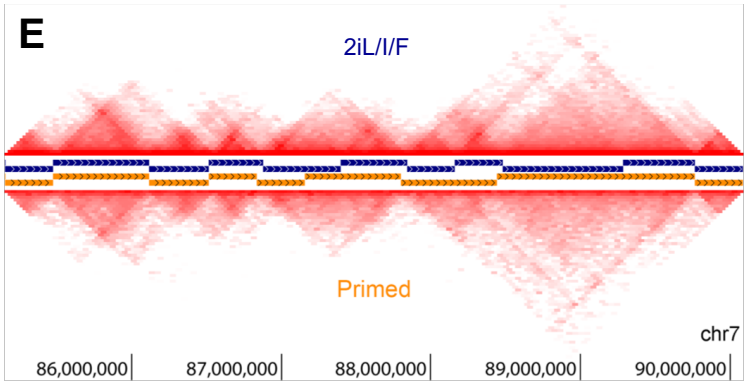

F

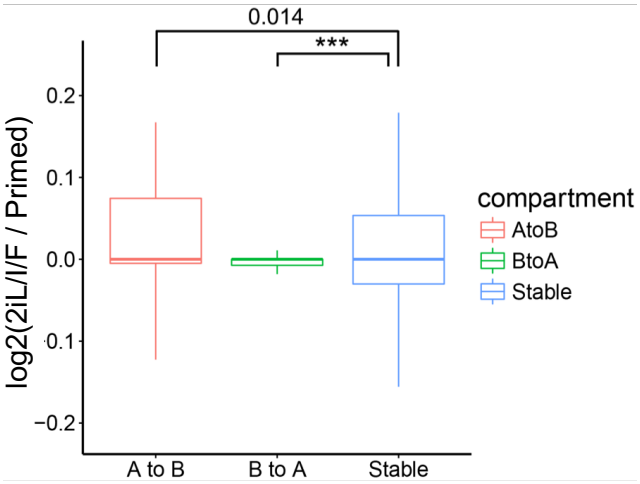

Figure S7: Hi-C libraries and TAD structure
(A) Summary of Hi-C sequencing read pairs and interactions in 2iL/I/F and primed hESCs. (B) Total counts of TADs and boundaries identified in 2iL/I/F and primed hESCs after discarding X and Y chromosome interactions. (C) Global size distributions of boundaries > 40 kb. (D) Bar chart of the number of Elf1 TADs within an H1 TAD and depiction of how "extra" TADs are defined. (E) Contact heatmaps of a region in chromosome 7. Navy and dark orange tracks denote TADs in 2iL/I/F and primed hESCs, respectively. (F) Boxplot of gene expression (RPKM) overlapping A to B compartment switches. "A to B" and "B to A" are 2iL/I/F to primed directions. Stable are compartments that do not switch. P-values are computed using two-sample t-test with one sided alternative. *** P-value < 1.34×10^{-10}.

Table S1: DEGs and DEG Pathways
List of differentially expressed genes and Gene Ontology pathways

Table S2

Elf1 2iL/I/F Sample	Number of Reads Sequenced	Mapped reads	Mapping Efficiency
ENK27acRep1	10,289,987	9,885,369	96.1%
ENK27acRep2	34,868,010	31,613,836	90.7%
ENK27me3Rep1	11,131,576	10,256,807	92.1%
ENK27me3Rep2	28,435,049	25,806,462	90.8%
ENK4me1Rep1	29,070,786	26,338,406	90.6%
ENK4me1Rep2	23,139,610	22,376,410	96.7%
ENK4me3Rep1	15,960,227	14,359,079	90.0%
ENK4me3Rep2	25,423,585	23,909,154	94.0%
ENK9me3Rep1	28,486,276	25,936,935	91.1%
ENK9me3Rep2	42,803,514	38,115,104	89.0%
ENInputRep1	31,149,021	23,377,765	75.1%
ENInputRep2	20,116,865	18,585,106	92.4%
Total 2iL/I/F (1.35E10 bases)		270,560,433	
Elf1 Transitioning Sample ID	Number of Reads Sequenced	Mapped reads	Mapping Efficiency
EPK27acRep1	16,542,791	15,466,596	93.5%
EPK27acRep2	19,045,610	14,495,788	76.1%
EPK27me3Rep1	14,661,174	12,484,843	85.2%
EPK27me3Rep2	17,360,465	10,303,499	59.4%
EPK4me1Rep1	13,466,280	12,643,726	93.9%
EPK4me1Rep2	14,628,581	13,524,908	92.5%
EPK4me3Rep1	14,142,256	12,502,355	88.4%
EPK4me3Rep2	12,112,327	9,124,628	75.3%
EPK9me3Rep1	37,350,962	32,818,042	87.9%
EPK9me3Rep2	42,244,794	36,811,767	87.1%
EPInputRep1	8,581,717	7,920,395	92.3%
EPInputRep2	37,772,483	35,291,325	93.4%
Total EP genome (1.07E10 bases)		213,387,872	

Table S2: Summary of Mapping Statistics for Elf1 2iL/I/F and Transitioning (AF) Cells
ChIP-seq DNA libraries were sequenced on Illumina platform, SE75 and mapped using Bowtie2.

Table S3

	H3K4me1		H3K4me3		H3K27ac		H3K27me3		H3K9me3		# enhancers after removing H3K4me3 overlapping peaks
	# peaks	% genome	# peaks	% genome	# peaks	% genome	# peaks	% genome	# peaks	% genome	
Elf1 2iL/I/F	116,999	9.25%	21,071	1.58%	67,500	4.49%	4,512	0.51%	12	0.00%	98,020
Elf1 TR	83,940	5.61%	20,541	1.29%	36,701	1.71%	17,379	1.09%	2,831	0.22%	69,467
H1 Primed	46,843	3.04%	22,866	1.41%	24,668	1.81%	10,454	1.39%	22,911	2.35%	38,677

Table S3: Number of ChIP-seq Peaks and Percent Genome covered by Histone Modification
Numbers in bar chart for Figure 2B. Number of ChIP-seq peaks called by MACS that pass FDR 5% for each cell type. Numbers in bar chart for Figure 2C. Percent of genome covered by each histone modification. Includes number of K4me1 peaks after excluding peaks that overlap K4me3.

Table S4: Enhancer overlaps with ENCODE DHS and Roadmap H3K4me1
Charts of the number or fraction of a cell type's peaks were found in 2iL/I/F, transitioning or primed hESCs from 177 ENCODE DHS cell types or 127 Roadmap Epigenome Project cell types.

Supplemental Experimental Procedures

Human Embryonic Stem Cell Culture

All human ESC culture conditions were as previously described (Sperber et al., 2015), with the following modifications. Base hESC media consisted of DMEM/F12, 20% knock-out serum replacer (KSR), 1mM sodium pyruvate, 0.1 mM nonessential amino acids, 50 U/mL penicillin, 50 ug/mL streptomycin, and 0.1mM β-mercaptoethanol. Growth conditions: 2iL/I/F - 1uM Mek inhibitor (PD0325901) [catalog #S1036, Selleck Chemicals, Houston, TX, USA], 1uM GSK3 inhibitor (CHIR-99021) [catalog #S2924, Selleck Chemicals, Houston, TX, USA], 10 ng/mL human Leukemia inhibitory factor [catalog #YSP1249, Speed Biosystems, Gaithersburg, MD, USA], 5ng/mL IGF-1 [catalog #100-11 Peprotech, Rocky Hill, NJ], 10ng/mL FGF [catalog #PHG0263, Thermo Fisher Scientific, Waltham, MA, USA]; 4iL/I/F - 1uM Mek inhibitor (PD0325901), 1uM GSK3 inhibitor (CHIR-99021), 5uM JNK inhibitor (SP600125) [catalog #S1460, Selleck Chemicals, Houston, TX, USA], 2uM p38 inhibitor (BIRB796) [catalog #S1574, Selleck Chemicals, Houston, TX, USA], 10 ng/mL Leukemia inhibitory factor, 5ng/mL IGF-1, 10ng/mL FGF.

Flow Cytometry for CD75 and CD77 Markers

2iL/I/F Elf1 cells were harvested from one 10cm^2 plate. The plate was rinsed with PBS, then cells were separated from the plate with trypsin. After the incubation, cells were unicellularized through pipetting of the cell suspension. Trypsin was neutralized using 5% FBS/PBS solution. Cells were rinsed with PBS twice and resuspended in 500 uL of 5% FBS/PBS. 5mL of a 70% EtOH solution was slowly added while cells were vortexed. Cells were stored at -20°C for two days.

To perform antibody staining, cells were removed from -20°C and washed twice with PBS. Cells were resuspended in 300uL of 5% FBS/PBS and then split equally into three samples: an unstained control, CD75 stained, and CD77 stained. 1ug of Anti-CD75 antibody (Abcam, cat #: ab77676, lot #: GR3181182-5) was added to the CD75 stained sample. 1ug of Anti-CD77 antibody (BD Biosciences, cat #: 551352, lot #: 7214648) was added to the CD77 stained sample. The control sample was stored at 4°C in 400uL 5% FBS/PBS. CD75 and CD77 samples were stained with the primary antibody for 30 minutes at room temperature, washed once with 5% FBS/PBS. They were then resuspended in 100uL of 5% FBS/PBS containing the secondary antibody, Alexa Fluor 586 donkey anti-mouse (Invitrogen, cat #: A10037, lot #: 1917938), at a dilution of 1:1000 and incubated for 30 minutes at room temperature in the dark. CD75 and CD77 samples were rinsed once with 5% FBS/PBS and resuspended in 400uL of 5% FBS/PBS. The control, CD75, and CD77 samples were fixed by adding 100uL 4% PFA and were mixed by pipetting. Flow cytometry was performed with BD FACSAria II. The program BD FACSDiva was used for gating and analysis.

Reduced Representation Bisulfite Sequencing

Genomic DNA was extracted with Qiagen All Prep Kit (Qiagen, cat #: 80204). Unmethylated lambda DNA was sheared to 300 bp using Covaris M-series and spiked in to each sample at 0.5% of DNA quantity. About 100-500 ng of genomic DNA was digested in a total volume of 20 uL with 1 uL MspI enzyme (NEB, cat #: R0106S) with 2 uL NEB buffer 2 and incubated at 37C for 2-4 hours, followed by heat inactivation at 65C for 10min. Next, samples underwent A-tailing reaction by adding 1.2 uL Klenow exo- (NEB, cat #: M0212S), 1.2 uL of dNTP mix (10mM dATP, 1mM dGTP, 1mM dCTP (NEB, cat #: N0446S)) to each sample and incubating at 30C for 30 min, then 37C for 30 min, followed by heat inactivation at 65C for 10min. Methylated Illumina compatible adapters with ligated to the DNA samples by adding to each sample 1.4 uL of NEB buffer 2, 1 uL of 10uM methylated adapters, 1.2 uL of T4 DNA ligase (NEB, cat #: M0202S), 3.4 uL of 10mM ATP, and sterile water to a final volume of 34 uL. The ligation reaction sat at RT for 1 hour. Ligated DNA samples were then gel size selected for 150-350 bp fragment size and then samples were proceeded to bisulfite conversion (MethylCode Bisulfite Conversion Kit, ThermoFisher, cat #: MECOV50). Converted DNA samples underwent indexing PCR using KAPA

HIFI Hotstart URACIL+ Readymix (Fisher Scientific, cat #: NC0682281) for 12-15 cycles. Final libraries were cleaned with AMPure beads at 1.1x ratio and sequenced on NextSeq 500. Samples were mapped using Bismarck(Krueger and Andrews, 2011) and methylation levels were calculated using Bismark Methylation Extractor. H9 data were taken from Kyttala et al., 2016 (Kyttala et al., 2016).

ChIP-seq Analysis and Visualization

ChIP-seq was performed and analyzed as previsously described (Hawkins et al., 2013; Valensisi et al., 2017). Sequencing raw reads were trimmed for low quality and adapters using TrimGalore!, aligned to genome (version hg19) using Bowtie2 (Langmead and Salzberg, 2012). For the UCSC genome browser tracks, ChIP-seq signals were normalized by RPKM followed by subtraction of input from ChIP using deepTools suite (Ramirez et al., 2014). Heatmaps and histograms are of normalized ChIP-seq signal: samples are normalized by read count and log2(chip reads/input reads) per 10kb bin is plotted using deepTools suite (Ramirez et al., 2014).

Peak Calling

ChIP-seq peaks were called on merged replicates and normalized to input using MACS v1.4 (Zhang et al., 2008). Peak calls with a FDR of 5% or less were used for downstream analysis. Percent of genome covered, also referred to as genomic space in text, was defined as total number of bases under the peak divided by 2.7e9, the effective genome size. This was found it to be a better representation of global chromatin structure (e.g. a 10kb region can be covered by one or many ChIP-seq peaks due to peak size; the number of peaks may vary more than the total number of bases under the peaks). Peak comparisons and overlaps were done using the BedTools suite (Quinlan and Hall, 2010) for autosomal chromosomes only.

In order to compare the histone marks (H3K4me1 and H3K27ac) across cell types, we divided the genome into 10 kb bins and counted the reads across these 10 kb genomic regions using *featurecounts* in Rsubread package (Liao et al., 2014). Then, PCA was performed on regularized log transformed read count data obtained using DESeq2 (Love et al., 2014).

RNA-seq and Gene Expression

Embryonic stem cells were counted and 200,000 cells were pelleted for RNA extraction using the Qiagen All Prep Kit (cat # 80204). RNA-seq libraries were constructed using the Scriptseq RNA-seq Library Preparation Kit on ¾ of total RNA. Libraries were sequenced single-end 75 on Illumina NextSeq. The quality of the reads and contamination of adapter sequences were checked with FastQC tool (http://www.bioinformatics.babraham.ac.uk/projects/fastqc/). Reads were mapped to human hg19 genome (UCSC) using TopHat2 (Kim et al., 2013). Transcript quantification was performed by Cufflinks (Trapnell et al., 2010) using GENCODE's comprehensive gene annotation release 19 as reference annotation.

Differential Gene Expression Analysis

The raw read counts were calculated using *featurecounts* in Rsubread package (Liao et al., 2014) and GENCODE's release 19 as reference annotation. Differential gene expression analysis was performed with DESeq2 (Love et al., 2014) using read counts matrix. Two sets of differentially expressed genes (DEGs) are identified with P-value < 0.01, log2FC > |1| and P-value < 0.01, log2FC > |2|. The P-values were adjusted for multiple hypothesis correction. DEGs in all pairwise sample comparisons were identified. PCA was performed on regularized log transformed read count data from autosomes of top 500 highly variant genes obtained using DESeq2(Love et al., 2014) and plot was generated using ggplot2 in R(Wickham, 2009).

For transposable elements (TE) analysis, transcripts were quantified using hg19 UCSC RepeatMasker TE annotation. We considered unique reads as well as multi mapped reads during quantification of TE

transcripts. PCA was performed on regularized log transformed read count data of top 500 highly variant TE transcripts obtained using DESeq2.

Identification of Overrepresented GO Terms and Enriched Pathways

ClueGO (Bindea et al., 2009) was used to identify the overrepresented GO terms and enriched pathways with the data from gene ontology consortium and KEGG pathways database. The input gene lists to the ClueGO were DEGs with P-value < 0.01, log2FC > |1|. We used all genes in the genome as background. The statistically significant GO terms and pathways were filtered with P-value < 0.05 and GO term/pathway should contain at least 5 DEGs. P-values were adjusted with Benjamini Hochberg method for multiple hypothesis correction.

Sankey Plot

We looked at promoter chromatin state transitions from 2iL/I/F to primed to gain insight into the establishment of bivalency and other chromatin state changes occurring at gene promoters. In order to accomplish this goal we focused on the over 19,000 autosomal protein-coding gene TSS annotated by GENCODE. We assigned a promoter to a gene if the H3K4me3 peak was within -2kb to +500bp of the TSS. Sankey plot is limited by the presence of multiple promoters within overlapping regions. Sankey plot were created using Google Charts (https://developers.google.com/chart/interactive/docs/gallery/sankey)

In situ DNase Hi-C

Samples were prepared in a manner similar to Deng et al. (Deng et al., 2015). Briefly, nuclei from ~5 x 106 cross-linked Elf1 cells were isolated and permeabilized, and chromatin was digested with 4 U DNase I at room temperature for 4 min. Following end-repair and dA-tailing reactions, chromatin ends were ligated to biotinylated bridge adapters, and nuclei were purified with two volumes of AMPure XP beads (Beckman Coulter). Chromatin ends were phosphorylated and ligated in situ, and protein-DNA cross-links were reversed by proteinase K digestion and incubation at 60C overnight. Following purification, DNA was sonicated to an average size of 400 bp, and chimeric species were enriched via pull-down with streptavidin-coated magnetic beads (Active Motif). Preparation of Hi-C libraries was accomplished by ligating sequencing adapters to the ends of bead-bound DNA fragments and PCR-amplifying the products in the presence of forward and barcoded reverse primers. Libraries were purified with AMPure XP beads, DNA concentrations were determined using a Qubit 2.0 (Thermo Fisher), and size distributions were quantified using a Bioanalyzer with a high sensitivity kit (Agilent). A 10 ng aliquot from each library was digested with BamHI, run on the Bioanalyzer, and compared to an undigested control in order to confirm the presence of a reconstituted BamHI site at the junctions of ligated bridge adapters.

Hi-C Sequencing and Data Processing

Raw Hi-C sequencing reads from H1 hESCs were downloaded from GEO (GSE35156). Reads were aligned using Bowtie2 (Langmead and Salzberg, 2012) to the hg19 reference genome and filtered for MAPQ ≥ 10, uninformative ligation products, and PCR duplicates using HiC-Pro (Servant et al., 2015).

Valid Hi-C read pairs from biological replicates of Elf1 and H1 hESCs were combined, respectively, and used to generate raw chromosome-wide interaction matrices binned at a resolution of 40kb. Raw matrices were ICE-normalized using the HiTC Bioconductor package (Servant et al., 2012) for R, and TADs and boundaries were identified using TopDom (Shin et al., 2016) with a window size of 5. X and Y chromosomes were removed for the datasets for all Hi-C analyses.

Insulation scores were calculated from the ICE-normalized matrices of both the Elf1 and H1 hESCs, separately. Insulation vectors were detected via cworld (Giorgetti et al., 2016) using the script matrix2insulation.pl, and using the following options: (--is 240000 --nt 0.1 --ids 160000 --im median --

bmoe 0). Differential insulation scores computing Elf1 score minus H1 score for the all autosomes via cworld using the script compareInsulation.pl, with inputs being the two insulation scores above.

High-Confidence SMC1 ChIA-PET interactions for naïve and primed hESCs were downloaded as a supplemental table (Ji et al., 2016). A ChIA-PET was considered to span a TAD if both PET termini were located within 40 kb of a TAD boundary.

Spatial compartments and activity status were identified via principal component analysis (PCA) using Homer Tools(Heinz et al., 2010). Processed Hi-C reads were imported into Homer. For each chromosome, a contact matrix was constructed at 40 kb resolution and normalized using a sliding window of 400 kb as background. Next, the correlation between intra-chromosomal contact profiles was computed and the first principal component (PC1) vector was extracted and saved as a bedGraph file. H3K27ac ChIP-seq peaks served as a seed for determining which regions are active (PC1 > 0). A genomic region was considered cell type-specific if it met the following three criteria: 1) the average PC1 value was positive in one cell type and negative in the other, 2) the difference in the average PC1 value was > 50 and 3) the correlation between contact profiles was < 0.4. Randomization was achieved by selecting coordinates from a pool of 40 kb regions that had associated PC1 values and were not located within any cell type-specific sub-compartments.

Supplemental References

Bindea, G., Mlecnik, B., Hackl, H., Charoentong, P., Tosolini, M., Kirilovsky, A., Fridman, W.H., Pages, F., Trajanoski, Z., and Galon, J. (2009). ClueGO: a Cytoscape plug-in to decipher functionally grouped gene ontology and pathway annotation networks. Bioinformatics *25*, 1091-1093.

Giorgetti, L., Lajoie, B.R., Carter, A.C., Attia, M., Zhan, Y., Xu, J., Chen, C.J., Kaplan, N., Chang, H.Y., Heard, E.*, et al.* (2016). Structural organization of the inactive X chromosome in the mouse. Nature *535*, 575-579.

Hawkins, R.D., Larjo, A., Tripathi, S.K., Wagner, U., Luu, Y., Lonnberg, T., Raghav, S.K., Lee, L.K., Lund, R., Ren, B.*, et al.* (2013). Global chromatin state analysis reveals lineage-specific enhancers during the initiation of human T helper 1 and T helper 2 cell polarization. Immunity *38*, 1271-1284.

Heinz, S., Benner, C., Spann, N., Bertolino, E., Lin, Y.C., Laslo, P., Cheng, J.X., Murre, C., Singh, H., and Glass, C.K. (2010). Simple combinations of lineage-determining transcription factors prime cis-regulatory elements required for macrophage and B cell identities. Mol Cell *38*, 576-589.

Ji, X., Dadon, D.B., Powell, B.E., Fan, Z.P., Borges-Rivera, D., Shachar, S., Weintraub, A.S., Hnisz, D., Pegoraro, G., Lee, T.I.*, et al.* (2016). 3D Chromosome Regulatory Landscape of Human Pluripotent Cells. Cell Stem Cell *18*, 262-275.

Kim, D., Pertea, G., Trapnell, C., Pimentel, H., Kelley, R., and Salzberg, S.L. (2013). TopHat2: accurate alignment of transcriptomes in the presence of insertions, deletions and gene fusions. Genome Biol *14*, R36.

Krueger, F., and Andrews, S.R. (2011). Bismark: a flexible aligner and methylation caller for Bisulfite-Seq applications. Bioinformatics *27*, 1571-1572.

Kyttala, A., Moraghebi, R., Valensisi, C., Kettunen, J., Andrus, C., Pasumarthy, K.K., Nakanishi, M., Nishimura, K., Ohtaka, M., Weltner, J.*, et al.* (2016). Genetic Variability Overrides the Impact of Parental Cell Type and Determines iPSC Differentiation Potential. Stem Cell Reports *6*, 200-212.

Langmead, B., and Salzberg, S.L. (2012). Fast gapped-read alignment with Bowtie 2. Nat Methods *9*, 357-359.

Liao, Y., Smyth, G.K., and Shi, W. (2014). featureCounts: an efficient general purpose program for assigning sequence reads to genomic features. Bioinformatics *30*, 923-930.

Love, M.I., Huber, W., and Anders, S. (2014). Moderated estimation of fold change and dispersion for RNA-seq data with DESeq2. Genome Biol *15*, 550.

Quinlan, A.R., and Hall, I.M. (2010). BEDTools: a flexible suite of utilities for comparing genomic features. In Bioinformatics, pp. 841-842.

Ramirez, F., Dundar, F., Diehl, S., Gruning, B.A., and Manke, T. (2014). deepTools: a flexible platform for exploring deep-sequencing data. Nucleic Acids Res *42*, W187-191.

Servant, N., Lajoie, B.R., Nora, E.P., Giorgetti, L., Chen, C.J., Heard, E., Dekker, J., and Barillot, E. (2012). HiTC: exploration of high-throughput 'C' experiments. Bioinformatics *28*, 2843-2844.

Servant, N., Varoquaux, N., Lajoie, B.R., Viara, E., Chen, C.J., Vert, J.P., Heard, E., Dekker, J., and Barillot, E. (2015). HiC-Pro: an optimized and flexible pipeline for Hi-C data processing. Genome Biol *16*, 259.

Shin, H., Shi, Y., Dai, C., Tjong, H., Gong, K., Alber, F., and Zhou, X.J. (2016). TopDom: an efficient and deterministic method for identifying topological domains in genomes. Nucleic Acids Res *44*, e70.

Trapnell, C., Williams, B.A., Pertea, G., Mortazavi, A., Kwan, G., van Baren, M.J., Salzberg, S.L., Wold, B.J., and Pachter, L. (2010). Transcript assembly and quantification by RNA-Seq reveals unannotated transcripts and isoform switching during cell differentiation. Nat Biotechnol *28*, 511-515.

Valensisi, C., Andrus, C., Buckberry, S., Jayavelu, N.D., Lund, R.J., Lister, R., and Hawkins, R.D. (2017). Epigenomic landscapes of hESC-derived neural rosettes: modeling neural tube formation and diseases. Cell Rep *20*, 1448-1462.

Wickham, H. (2009). ggplot2: Elegant Graphics for Data Analysis. In (Springer-Verlag New York).

Yan, L., Yang, M., Guo, H., Yang, L., Wu, J., Li, R., Liu, P., Lian, Y., Zheng, X., Yan, J.*, et al.* (2013). Single-cell RNA-Seq profiling of human preimplantation embryos and embryonic stem cells. Nat Struct Mol Biol *20*, 1131-1139.

Zhang, Y., Liu, T., Meyer, C.A., Eeckhoute, J., Johnson, D.S., Bernstein, B.E., Nusbaum, C., Myers, R.M., Brown, M., Li, W.*, et al.* (2008). Model-based analysis of ChIP-Seq (MACS). Genome Biol *9*, R137.